Clathrin-independent endocytosis and retrograde transport in cancer cells promote cytotoxic CD8 T cell activation

Xu, Shiqiang; Buridant, Alix; Hirsch, Thibault; Shafaq-Zadah, Massiullah; Dransart, Estelle; Ledoux, Benjamin; Johannes, Ludger; van der Bruggen, Pierre; Morsomme, Pierre; Renard, Henri-François

Published in:
eLife

DOI:
10.7554/eLife.105821.1

Publication date:
2025

Document Version
Early version, also known as pre-print

Cell Biology
Immunology and Inflammation

Clathrin-independent endocytosis and retrograde transport in cancer cells promote cytotoxic CD8 T cell activation

Reviewed Preprint
v1 • February 17, 2025
Not revised

Shiqiang Xu, Alix Buridant, Thibault Hirsch, Massiullah Shafaq-Zadah, Estelle Dransart, Benjamin Ledoux, Ludger Johannes, Pierre van der Bruggen, Pierre Morsomme, Henri-François Renard

UNamur, Namur Research Institute in Life Sciences, Research Unit in Cell Biology, Namur, Belgium • UCLouvain, Louvain Institute of Biomolecular Science and Technology, Group of Molecular Physiology, Louvain-la-Neuve, Belgium • UCLouvain, de Duve Institute, Bruxelles, Belgium • Institut Curie, PSL Research University, Cellular and Chemical Biology unit, U1143 INSERM, UMR3666 CNRS, Paris, France • UNamur, Morph-Im Platform, Namur, Belgium • WELBIO, Wavre, Belgium

eLife Assessment

This **valuable** study provides **convincing** evidence that specific proteins on the surface of cancer cells undergo a particular form of recycling and are redirected toward the cell-cell contact with T cells, a type of immune cell. However, the characterization of the consequences of T cell activation resulting from perturbing the recycling pathway is **incomplete**. Furthermore, relevant literature has not been sufficiently cited.

https://doi.org/10.7554/eLife.105821.1.sa3

Abstract

Endophilin A3-mediated clathrin-independent endocytosis (EndoA3-mediated CIE) mediates the internalization of immunoglobulin-like proteins, including key immune synapse components. Here, we identify ICAM1 as a novel EndoA3-dependent cargo, alongside ALCAM. We demonstrate that both proteins subsequently undergo retromer-dependent retrograde transport to the *trans*-Golgi network (TGN) in cancer cells. From there, they undergo polarized redistribution to the plasma membrane, where they contribute to immune synapse formation between cancer cells and cytotoxic CD8 T cells. Disruption of EndoA3 or retromer components significantly impairs the activation of autologous cytotoxic CD8 T cells, as demonstrated by decreased cytokine production. Concomitantly, we observed a reduced localization of ICAM1 at the immune synapse, indicating impaired immune synapse integrity. Indeed, cancer cells lacking EndoA3-mediated CIE or retromer form enlarged immune synapses that fail to restore full T cell activation, suggesting a compensatory attempt by T cells to overcome the defective synapse. Together, these findings reveal that EndoA3-mediated CIE and retrograde transport act in concert in cancer cells to relocate immune

synapse components via the Golgi, thereby promoting the activation of cytotoxic CD8 T cells. Our study paves the way for the design of future therapeutic strategies targeting these pathways to enhance T cell-mediated anti-tumor immunity.

Significance Statement

This study uncovers a novel mechanism by which clathrin-independent endocytosis (CIE) and retrograde transport collaborate to regulate immune synapse dynamics in cancer cells. We identify ICAM1 as a new cargo of Endophilin A3-mediated CIE, highlighting its role in the polarized redistribution of immune synapse components critical for cytotoxic CD8 T cell activation. By linking a specific CIE mechanism and retrograde transport to immune synapse function, our findings provide new insights into cancer-immunity interactions and suggest potential therapeutic strategies to enhance immune responses by targeting protein trafficking pathways.

Introduction

Endocytosis is a fundamental physiological process involving membrane bound carrier-mediated internalization of extracellular substances and cell membrane components into the cytoplasm. This process is essential for maintaining plasma membrane homeostasis and regulating signal transduction. Broadly, endocytosis can be classified into conventional clathrin-mediated endocytosis (CME) and unconventional clathrin-independent endocytosis (CIE). While CME has been extensively characterized, CIE remains less understood and complex as it includes several distinct endocytic mechanisms (1, 2). Following endocytosis, internalized cargoes are sorted in early/sorting endosomes, where they are either directed toward lysosome for degradation or recycled to the plasma membrane for further activity. Some are recycled directly to the plasma membrane via Rab4/Rab11 recycling endosomes (3, 4), while others are retrieved by retromer or Commander complexes for transport to the *trans*-Golgi network (TGN), a process termed retrograde transport (5–8). Increasing evidence has linked retrograde transport to the maintenance of cell polarity (9). For instance, β_1 integrins are transported to the TGN via the retrograde transport route post-endocytosis, where they are re-secreted in a polarized manner to the leading edge of migrating cells, supporting front-rear polarity crucial for persistent migration (10). Similarly, in T cells, adaptor molecules such as the Linker for Activation of T cells (LAT) are transported to the TGN after endocytosis and redistributed to the immune synapse (11). The immune synapse is a polarized structure formed between immune and target cells (*e.g.*, cytotoxic CD8 T cells and cancer cells) (12), which exemplifies the intricate interplay between retrograde transport and cell polarity. Despite its importance, the connection between specific CIE mechanisms and retrograde transport in polarized cellular contexts remains largely underexplored.

Endophilin A (EndoA) proteins are key players in endocytosis, belonging to the BAR (Bin/Amphiphysin/Rvs) domain protein family known for their ability to sense and/or induce membrane curvature (13, 14). Mammalian cells express three isoforms of EndoA: EndoA1, A2, and A3 (15, 16). EndoA1 is predominantly expressed in brain, EndoA3 is abundant in both brain and testes, and EndoA2 is ubiquitously expressed across tissues (17, 18). Initially, EndoA proteins were implicated in CME in neuronal cells, where they recruit dynamins and synaptojanins via interactions between their Src-homology 3 (SH3) domains and proline-rich domains (PRDs), facilitating vesicle scission (19, 20) and subsequent clathrin uncoating (21, 22).

Recent studies have identified EndoA proteins as central players in clathrin-independent Fast Endophilin-Mediated Endocytosis (FEME) (23). EndoA2 has also been implicated in membrane scission events during the clathrin-independent uptake of Shiga and cholera toxins (24, 25). Intriguingly, the three EndoA isoforms are not fully functionally redundant in CIE. Only EndoA3, and not EndoA1 or A2, mediates the endocytosis of the immunoglobulin (Ig)-like protein ALCAM (Activated Leukocyte Cell Adhesion Molecule). The endocytosis of ALCAM, the first identified EndoA3-specific cargo, operates in an EndoA3-dependent manner and is driven by extracellular Galectin-8 and glycosphingolipids, in agreement with the glycolipid-lectin (GL-Lect) endocytosis mechanism (26–28). Another Ig-like protein, L1 Cell Adhesion Molecule (L1CAM, alternative name CD171), has since been confirmed as a cargo for EndoA3-mediated CIE (29).

ALCAM (CD166) is an adhesion molecule broadly expressed across tissues and overexpressed in various cancers, including bladder, prostate and colorectal carcinomas (30–32). ALCAM mediates cell-cell interactions either through homophilic binding with other ALCAM molecules (33) or by heterophilic binding with CD6 (34). CD6, a member of the scavenger receptor cysteine-rich (SRCR) protein family, is predominantly expressed in immune cells, particularly T lymphocytes, and in certain neuronal cells (35, 36). The ALCAM-CD6 interaction has been shown to play a critical role in immune synapse formation, providing essential co-stimulatory signals for optimal T cell activation and proliferation (37–39).

Given the polarized nature of the immune synapse, we hypothesized that EndoA3-mediated endocytosis in cancer cells could influence immune synapse formation through the subsequent retrograde transport and polarized redistribution of its components, such as ALCAM. Morevover, since both ALCAM and L1CAM are Ig-like proteins, we speculated that EndoA3-mediated endocytosis might preferentially facilitate the uptake of Ig-like proteins. Interestingly, Intercellular Adhesion Molecule 1 (ICAM1, alternative name CD54), a well-characterized immune synapse component critical for co-stimulating T cell activation via its interaction with Lymphocyte Function-associated Antigen 1 (LFA-1) on the T cells (40–42), is also an Ig-like protein. This prompted us to investigate whether ICAM1 serves as an EndoA3-dependent CIE cargo in cancer cells and whether its role in immune synapse formation relies on EndoA3-mediated CIE and retrograde transport.

Through a combination of cell biology and immunology experiments, we identify ICAM1 as a novel EndoA3-dependent endocytic cargo. Furthermore, we demonstrate that both ALCAM and ICAM1 undergo retromer-dependent retrograde transport to the TGN following EndoA3-mediated internalization. Disruption of EndoA3-mediated endocytosis or retromer-dependent retrograde transport in cancer cells significantly impairs the activation of autologous cytotoxic CD8 T cells, as evidenced by reduced cytokine production. This effect likely arises from the disrupted polarized redistribution of immune synapse components, including ICAM1, from the Golgi to the plasma membrane. Consistent with this hypothesis, we find that disrupting EndoA3-mediated endocytosis in cancer cells reduces ICAM1 recruitment to the immune synapse, compromising its structural integrity and formation. Interestingly, depleting EndoA3 or VPS26A increases the size of immune synapses, suggesting a compensatory mechanism in which T cells expand their contact area with cancer cells to counteract the decrease of correctly localized components. However, this adaptation ultimately fails to fully restore CD8 T cell activation. Collectively, our findings establish an unexplored functional connection between EndoA3-mediated clathrin-independent endocytosis, retrograde transport, and immune synapse dynamics in a polarized cellular context.

Results

ALCAM and ICAM1 are cargo clients of retromer-dependent retrograde trafficking

ALCAM and ICAM1 are known components of immune synapses (37–39, 41, 42). Given the polarized nature of these structures and the previously reported connection between retrograde transport and cell polarity (10, 11), we investigated whether ALCAM and ICAM1 serve as cargoes for retrograde transport. To address this question, we employed a SNAP-tag-based assay to study retrograde transport of cargoes from the plasma membrane to the Golgi apparatus (43) (**Fig. 1A**). Briefly, benzylguanine (BG)-labelled cargo-specific antibodies (IgG) were incubated with cells stably expressing the Golgi-resident Galactosyltransferase protein (GalT) fused to GFP and SNAP-tag (GalT-GFP-SNAP). If the cargo follows the retrograde route after endocytosis, it will be delivered to the TGN along with the BG-labelled antibody. Upon reaching the TGN, BG covalently reacts with the SNAP-tag, generating a large complex (IgG-SNAP-GFP-GalT), which can be immunopurified and analyzed by Western blot.

We used a HeLa cell line stably expressing the Golgi-resident SNAP-tag construct (HeLa GalT-GFP-SNAP), previously validated in earlier studies (10, 44). Additionally, we generated a LB33-MEL cell line stably expressing the same Golgi-resident SNAP-tag construct (LB33-MEL GalT-GFP-SNAP, Fig. S1A-B). Of note, the LB33-MEL melanoma cell line was derived from a melanoma patient (LB33) in 1988. A specific autologous CD8+ T cell line targeting this melanoma, obtained from the same patient, enables *in vitro* reconstitution of immune synapses (45). First, we validated the SNAP-tag functionality in both cell lines using the SNAP-Cell® TMR-Star reagent (**Fig. 1B** for HeLa; Fig. S1A for LB33-MEL). We observed a strong and specific colocalization of TMR-Star with the GFP signal of the SNAP-tag constructs in both cell lines. Second, immunofluorescence experiments showed that the SNAP-tag construct co-distributes with the *TGN*-specific marker TGN46 in LB33-MEL cells, confirming its correct and specific localization (Fig. S1B).

The retromer complex, composed of VPS26, VPS29 and VPS35 subunits in mammalian cells, is the best-studied machinery for retrograde transport (5, 46). Two paralogues of VPS26 subunit exist: VPS26A, expressed in most tissues, and VPS26B, mainly enriched in the brain (47, 48). To determine whether ALCAM and ICAM1 are cargoes of the canonical retromer complex, we conducted SNAP-tag-based retrograde transport assays in HeLa and LB33-MEL cell lines where VPS35 or VPS26A was knocked down by RNA interference (**Fig. 1C-D**, S1C for HeLa; Fig. S1D-E for LB33-MEL). BG-labelled anti-ALCAM or anti-ICAM1 antibodies were added to the cell culture medium for a 4-hour continuous uptake and the production of a covalent IgG-SNAP-GFP-GalT complex was monitored by Western blot (simplified as SNAP signal).

We observed that both ALCAM and ICAM1 are retrograde transport cargoes in cells treated with negative control siRNA, as IgG-SNAP-GFP-GalT complexes were detected by Western blot after incubation with BG-labelled antibodies (band ~ 210 kDa; **Fig. 1C-D** for HeLa; Fig. S1D for LB33-MEL). As a negative control, unlabeled antibodies (IgGs) showed no detectable SNAP signal in Western blot (**Fig. 1C**). Interestingly, depletion of VPS35 or VPS26A caused a significant reduction in the SNAP signal for both cargoes (**Fig. 1C-D**, S1C for HeLa; Fig. S1D-E for LB33-MEL). Of note, VPS26A depletion resulted in a stronger decrease in retrograde transport efficiency compared to VPS35 (**Fig. 1C-D**).

To explore additional factors involved in retrograde transport, we examined the role of Rab6 GTPase, a critical molecular player in secretion which controls the formation of membrane tubules originating from the TGN (49, 50). Disrupting Rab6 indirectly inhibits retrograde transport to the TGN of cargoes requiring subsequent polarized redistribution (10). Interestingly, Rab6 depletion impaired retrograde transport of ALCAM to the TGN, showing effects similar to retromer component depletion (Fig. S1F-G).

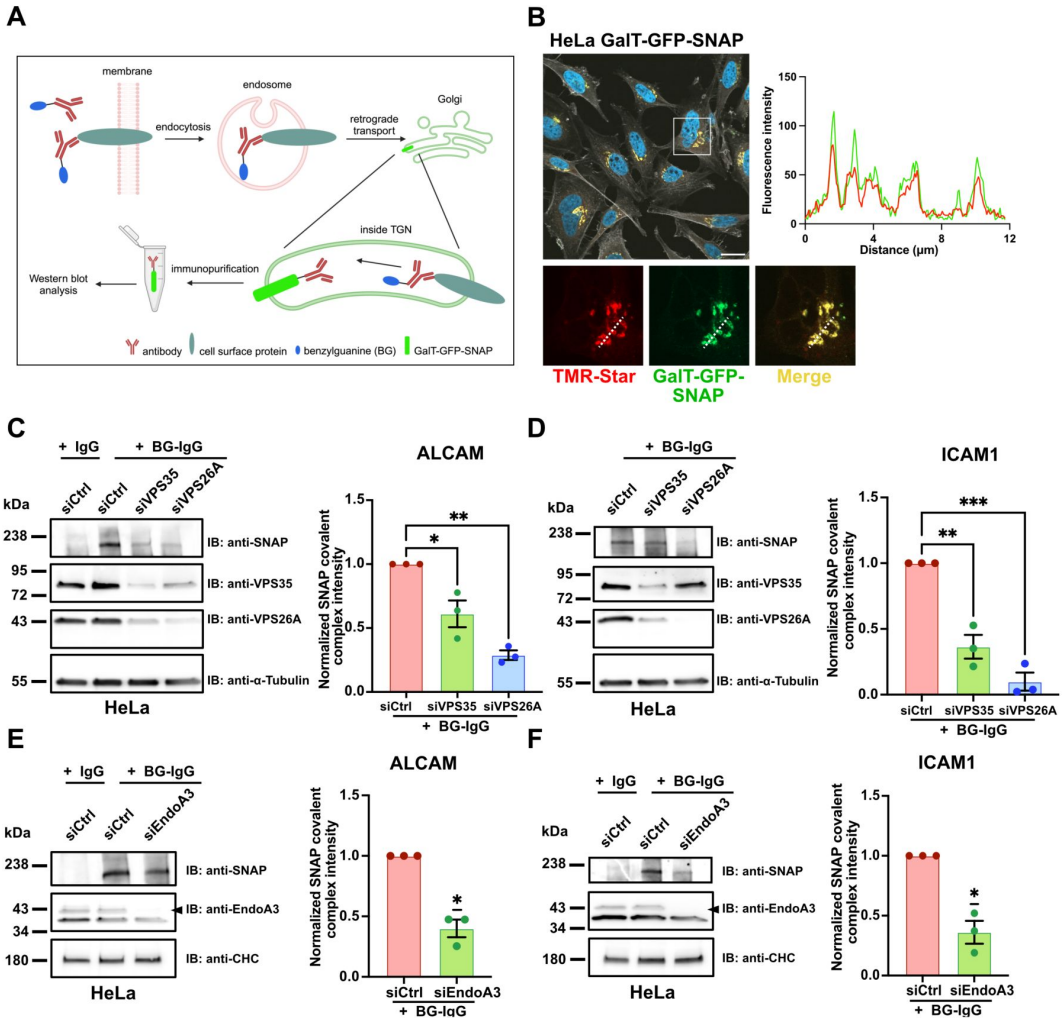

Figure 1.

Immune synapse components ALCAM and ICAM1 are retrograde transport cargoes that rely on EndoA3 and retromer

A Illustration of the SNAP-tag-based BG-labelled antibody uptake assay to study membrane protein endocytosis and retrograde transport.

B Confocal images of GalT-GFP-SNAP (green) and TMR-Star (red) in HeLa cells stably expressing the Golgi-resident GFP-fused SNAP-tag construct (HeLa GalT-GFP-SNAP). Actin (phalloidin, white) and nuclei (DAPI, blue) were also stained. Fluorescence intensity profile was made along the dashed line region in enlarged cropped area, and shows the colocalization of both signals. Scale bar: 20 µm.

C-F Retrograde transport of ALCAM and ICAM-1. Continuous BG-labelled anti-ALCAM (C and E) and anti-ICAM1 (D and F) antibody uptake for 4h at 37°C in HeLa GalT-GFP-SNAP cells. (C-D) Western blot analysis of HeLa GalT-GFP-SNAP cells transfected for 72h with siRNAs: negative control (siCtrl) or against retromer subunits (siVPS35 and siVPS26A). Immunodetection made with anti-SNAP, anti-VPS35, anti-VPS26A and anti-α-Tubulin (loading control) antibodies. Quantification of the covalent IgG-SNAP-GFP-GalT complex is shown as fractions of siCtrl condition (histogram). Quantification of VPS35 and VPS26A depletion is shown in Fig. S1C. (E-F) Western blot analysis of HeLa GalT-GFP-SNAP cells transfected for 72h with siRNAs: negative control (siCtrl) or against EndoA3 (siEndoA3). Immunodetection made with anti-SNAP, anti-EndoA3 and anti-clathrin heavy chain (CHC, loading control) antibodies. Quantification of the covalent IgG-SNAP-GFP-GalT complex (IB:anti-SNAP) is shown as fractions of siCtrl condition (histogram). Quantification of EndoA3 depletion is shown in Fig. S1H.

Data information: In (B), images are from a single experiment. Quantification data (C-F) are pooled from three independent experiments. Data are presented as mean ± SEM. *P < 0.05, **P < 0.01, ***P < 0.001 (C-D, RM one-way ANOVA with Dunnett's multiple comparison test; E-F, one sample *t* test). Source data are available online for this figure.

Together, these data demonstrate that retromer-mediated retrograde transport is critical for trafficking ALCAM and ICAM1 to the Golgi and that this process requires the full secretory capacity of the TGN.

Importantly, previous studies from our lab demonstrated that the endocytosis of ALCAM is mediated by EndoA3-dependent CIE (26, 51). We therefore investigated whether EndoA3 depletion could affect the post-endocytic retrograde transport of ALCAM to the TGN. To test this, we depleted EndoA3 in HeLa cells using RNA interference (**Fig. 1E-F**, S1H) and observed 60% of reduction in the IgG-SNAP signal intensity (**Fig. 1E**). Additionally, we performed retrograde transport assays with BG-labelled anti-ALCAM antibodies in the SNAP-tag-expressing LB33-MEL cell line (Fig. S1I). Since LB33-MEL cells do not express detectable levels of EndoA3 as confirmed by Western blot (26), we transiently transfected these cells with an EndoA3-GFP expression plasmid. Remarkably, EndoA3 expression increased the SNAP signal by ~50% compared to the control condition where cells were transfected with a plasmid expressing free GFP (Fig. S1I). Given that ICAM1 is also a member of the Ig-like protein family, we investigated whether the retrograde transport of this cargo depends on EndoA3. Interestingly, EndoA3 depletion in HeLa cells resulted in a significant reduction of the ICAM1 IgG-SNAP signal by 64% (**Fig. 1F**), comparable to the effect observed for ALCAM (**Fig. 1E**).

Collectively, these results suggest that: (i) ICAM1 is potentially a novel EndoA3-dependent cargo, (ii) substantial fractions of ALCAM and ICAM1 are transported to the TGN in a retromer-dependent manner after EndoA3-mediated CIE, and (iii) reintroducing EndoA3 in EndoA3-negative cells enhances the retrograde transport of these cell adhesion molecules to the TGN. These findings underscore a tight functional link between a specific clathrin-independent endocytic mechanism – mediated by EndoA3 – and the subsequent retrograde transport of cargoes to the TGN.

EndoA3 expression enhances the internalization of immune synapse components ALCAM and ICAM1 in cancer cells

To further confirm that ICAM1 is an EndoA3-dependent cargo, we employed live-cell TIRF imaging to directly observe the dynamics of EndoA3 and ICAM1 at the plasma membrane of both HeLa and LB33-MEL cell lines stably expressing EndoA3-GFP. Of note, the EndoA3-GFP-expressing HeLa cell line was generated and validated in earlier studies from our lab (26, 29), while the EndoA3-GFP-expressing LB33-MEL cell line (hereafter referred to as LB33-MEL EndoA3+) was developed specifically for this study. Both cell lines were then transiently transfected to express ICAM1-mScarlet.

Interestingly, EndoA3-GFP formed circular structures around ICAM1 patches in both cell lines (**Fig. 2A-B**, white arrows; Movie S1-2), and ICAM1 signals gradually disappeared from the plasma membrane (**Fig. 2A-B**; Movie S1-2). In addition, ICAM1-positive punctate structures were observed, where EndoA3-GFP was recruited before both protein signals disappeared from the cell surface (**Fig. 2B**, kymograph; Movie S3), indicating active endocytic events. This behavior mirrors TIRF observations previously reported for other EndoA3-dependent endocytic cargoes, such as ALCAM and L1CAM (26, 29). Moreover, we frequently observed EndoA3-GFP-positive punctate (Fig. S2A, white arrowheads; Movie S4) or tubular structures (Fig. S2B, white arrowheads; Movie S5) detaching from the tips or edges of continuously shrinking ICAM1 patches, further supporting the occurrence of endocytic events. Collectively, these observations confirm that ICAM1 is a novel EndoA3-dependent endocytic cargo.

To investigate the role of EndoA3-dependent CIE and subsequent retrograde transport in cancer cells on the activation of cytotoxic CD8 T lymphocytes, we further used the LB33-MEL cellular model. This cell line expresses a mutated antigenic peptide encoded by the *MUM3* gene. The MUM-3 peptide is presented on the cell surface by HLA-A*68012 molecules, an HLA-A28 subtype specific to patient LB33 (45, 52). A CD8 T cell line targeting the MUM-3 peptide, derived from the same

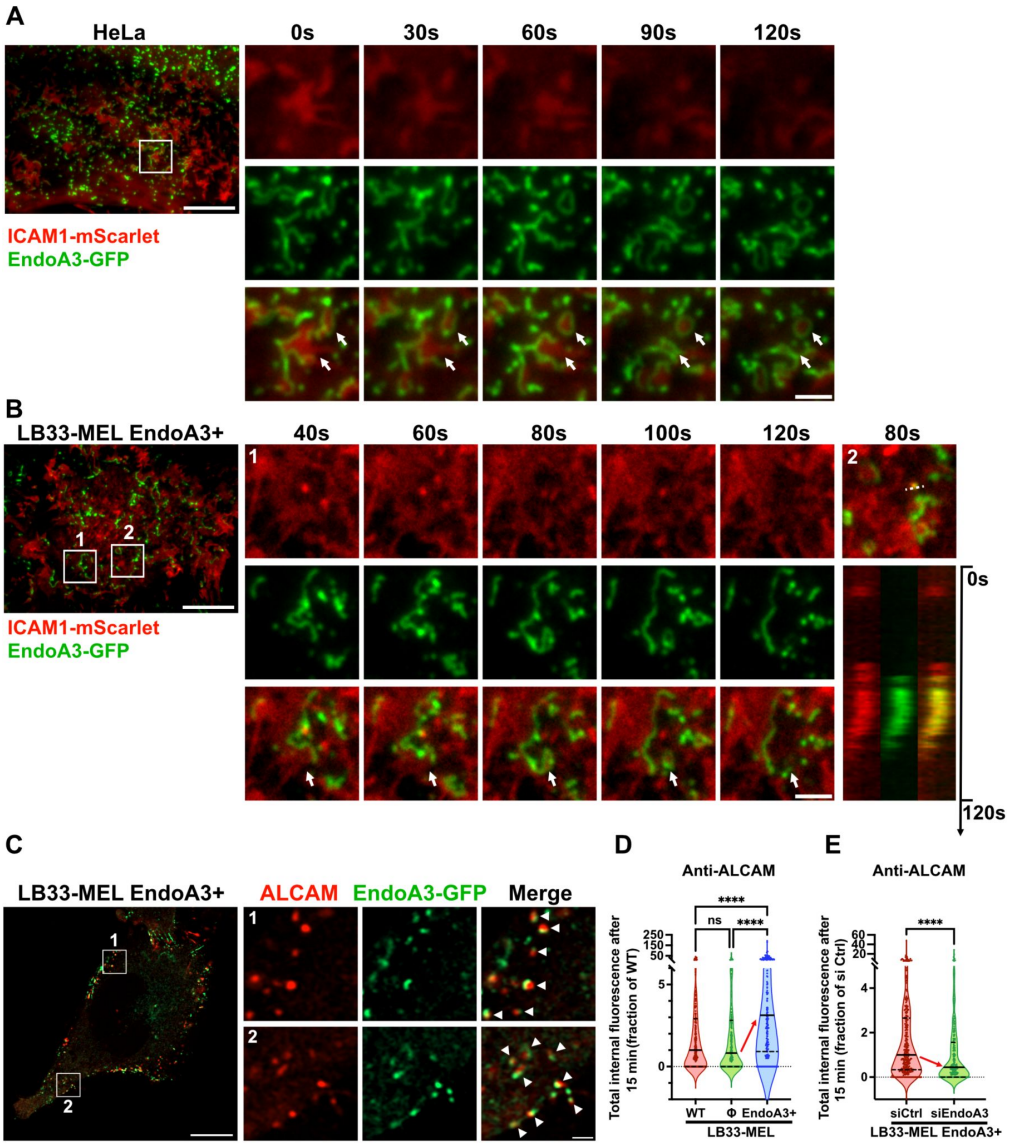

Figure 2.

EndoA3-dependent CIE mediates the uptake of immune synapse components ALCAM and ICAM1 in cancer cells

A-B Live-cell TIRF images of EndoA3-GFP (stable) and ICAM1-mScarlet (transient) in HeLa (A) and LB33-MEL (B) cells. Time series show enlarged cropped areas extracted from Movie S1 (A) and Movie S2 (B). White arrows indicate dynamic co-distribution of both signals. Kymograph in (B) was made along dashed line region in the 2nd cropped area (B; Movie S3). Scale bars: 10 µm (full size image), 2 µm (enlarged cropped areas).

C-E Continuous uptake of anti-ALCAM antibody for 15 min at 37°C in the following LB33-MEL cell lines: wild-type (WT, D), stably transfected with empty plasmid (Φ, D), or stably expressing EndoA3-GFP (LB33-MEL EndoA3+, C-E). In (E), cells were transfected with siRNAs: negative control (siCtrl) or against EndoA3 (siEndoA3). Quantification of EndoA3 depletion by western blots in Fig. S3A. (C) Airyscan images of Anti-ALCAM (red) and EndoA3-GFP (green). White arrowheads show colocalization between ALCAM and EndoA3. Scale bars: 10 µm (full size image), 1 µm (enlarged cropped areas). (D-E) Quantifications of anti-ALCAM internalization, expressed as fractions of WT condition (D) or siCtrl condition (E). (D) n cells: WT, n = 270; Φ, n = 279; EndoA3+, n = 274. (E) n cells: siCtrl, n = 350; siEndoA3, n = 234. Representative image examples in Fig. S3B-C.

Data information: All images (A-C) are representative of two independent experiments. In (D-E), data are pooled from three independent experiments. Data are presented as median and quartiles. ns, not significant. ****P < 0.0001 (D, Kruskal-Wallis test with Dunn's multiple comparison test; E, Mann-Whitney test). Source data are available online for this figure.

patient in 1990 (45), can form immune synapses with LB33-MEL cells *in vitro*. Although LB33-MEL cells lack detectable levels of EndoA3 (26), we have observed above that exogenous expression of EndoA3 enhances the retrograde transport of cell adhesion molecules (Fig. S1J).

Consistent with this result, high resolution Airyscan confocal images showed a clear colocalization between EndoA3-GFP and ALCAM, after a 15-minute uptake of anti-ALCAM antibodies in LB33-MEL EndoA3+ cells (**Fig. 2C**, white arrowheads). This observation confirmed further that this cell line recapitulates EndoA3-mediated endocytosis. Additional quantitative analyses revealed that the uptake of anti-ALCAM antibodies was three times higher in LB33-MEL EndoA3+ cells compared to wild-type or empty plasmid-transfected LB33-MEL cells (**Fig. 2D**, S3A). In addition, we performed a reverse-rescue uptake assay in LB33-MEL EndoA3+ cells transfected with EndoA3 siRNAs (**Fig. 2E**, S3B). ALCAM uptake was significantly reduced by 55% upon EndoA3 knockdown (**Fig. 2E**). Of note, exogenously expressed EndoA3-GFP protein was efficiently knocked down by siRNAs in LB33-MEL EndoA3+ cells, with an 80% reduction as shown by immunoblotting (Fig. S3C).

Taken together, these findings confirm that LB33-MEL EndoA3+ cells recapitulate functional EndoA3-dependent CIE, enhancing the uptake of canonical EndoA3-dependent cargoes. This cell line provides a robust model to assess the effects of EndoA3-mediated CIE and subsequent retrograde transport on CD8 T cell activation.

EndoA3-dependent CIE and retromer-mediated retrograde transport in cancer cells regulate cytotoxic CD8 T cell activation

Based on our results and considering that ALCAM and ICAM1 are key components of immune synapses, we hypothesized that their clathrin-independent endocytosis and subsequent retrograde transport might influence CD8 T cell activation. To test this hypothesis, we conducted CD8 T cell stimulation assays using LB33-MEL cells, in the presence or absence of EndoA3. Specifically, LB33-MEL EndoA3+ cells were treated with either control or EndoA3-targeting siRNAs before being co-cultured with CD8 T cells. Flow cytometry was then used to assess intracellular cytokine production in T cells (**Fig. 3A**).

Interestingly, when CD8 T cells were stimulated with EndoA3-depleted LB33-MEL cells, there was a significant decrease in both the percentage of T cells producing interleukin-2 (IL-2) and tumor necrosis factor α (TNFα) (**Fig. 3B**, upper and middle panels) and the absolute amounts of these cytokines (**Fig. 3C**, upper and middle panels), compared to CD8 T cells stimulated with LB33-MEL EndoA3+ cells. Although the percentage of T cells producing interferon γ (IFNγ) remained unchanged (**Fig. 3B**, bottom panel), the absolute amount of IFNγ produced was still significantly reduced (**Fig. 3C**, bottom panel). Of note, the efficiency of EndoA3-GFP depletion was confirmed by flow cytometry (Fig. S4A).

Next, we performed IFNγ secretion assays, where CD8 T lymphocytes were stimulated with differentially treated LB33-MEL cells. The supernatant was then analyzed using enzyme-linked immunosorbent assay (ELISA) (**Fig. 3D**). Wild-type, empty plasmid control, and EndoA3-GFP-expressing LB33-MEL cells all stimulated CD8 T cells to secrete IFNγ, compared to the control condition where T cells were kept alone (**Fig. 3E**). However, LB33-MEL EndoA3+ cells significantly enhanced CD8 T cell activation, with T cells secreting approximately 70% more IFNγ than those stimulated with wild-type or empty plasmid-transfected cells (**Fig. 3E**). This effect was lost when EndoA3 was depleted from LB33-MEL EndoA3+ cells using RNA interference (**Fig. 3E**).

Together with our previous results, these observations support the hypothesis that EndoA3-mediated CIE in cancer cells influences retrograde transport and the subsequent polarized redistribution of immune synapse components, such as ALCAM and ICAM1, thereby affecting T

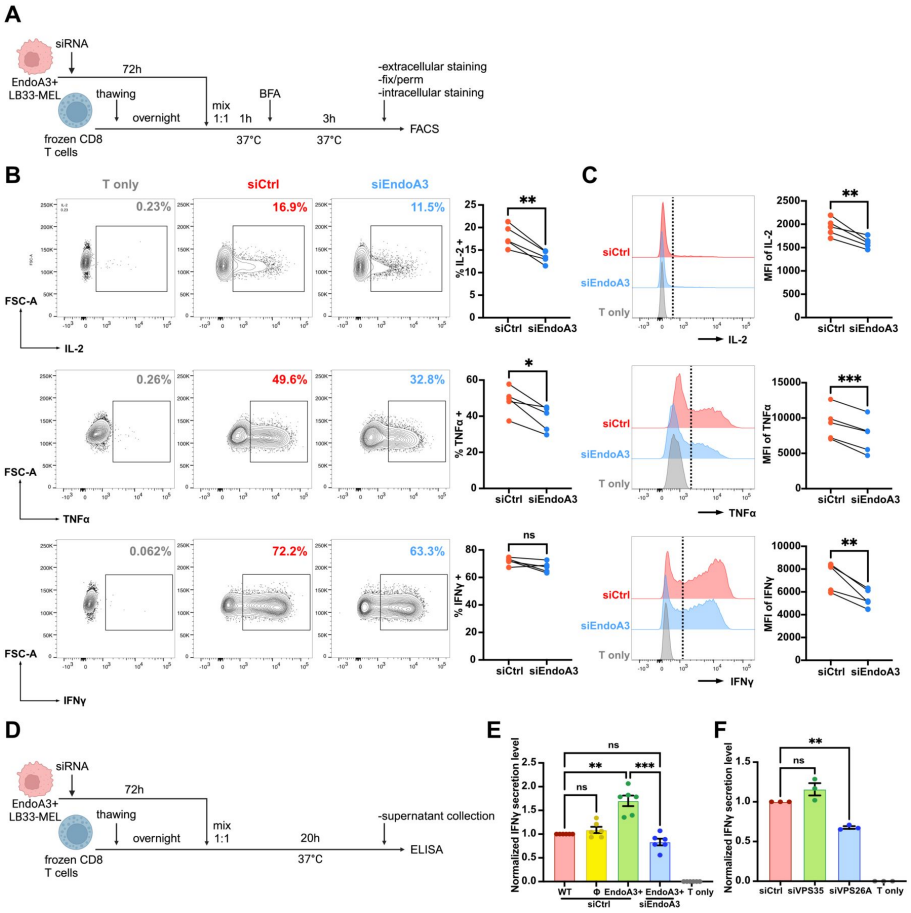

Figure 3.

Inhibition of EndoA3-dependent endocytosis and retrograde transport impairs T cell activation

A Scheme of flow cytometry analysis of cytokine production inside CD8 T cells stimulated by siRNA transfected EndoA3+ LB33-MEL cells.

B-C Flow cytometry analysis of CD8 T cell intracellular cytokine production after co-culture for 4h at 37°C with: no LB33-MEL (T only), EndoA3+ LB33-MEL transfected with negative control siRNA (siCtrl) or with siRNA against EndoA3 (siEndoA3). Quantification of EndoA3 depletion is shown in Fig. S4A. (B) Representative examples and quantifications (scatter plots) of the percentages of cytokine producing CD8 T cells (up, IL-2; middle, TNFα; bottom, IFNγ) after being stimulated by siCtrl or siEndoA3 treated LB33-MEL EndoA3+ cells. (C) Representative examples and quantifications (scatter plots) of the absolute amount of cytokines produced by CD8 T cells (up, IL-2; middle, TNFα; bottom, IFNγ; presented as median fluorescence intensity, MFI) after stimulation by siCtrl or siEndoA3 treated LB33-MEL EndoA3+ cells.

D Scheme of ELISA analysis of cytokine secretion from CD8 T cells stimulated with siRNA transfected EndoA3+ LB33-MEL cells.

E Quantification of IFNγ secretion (detected by ELISA) from CD8 T cells, cultured alone (T only) or co-cultured for 20h with the following LB33-MEL cell lines: wild-type LB33-MEL cells (WT), LB33-MEL cells stably transfected with empty (Φ) or EndoA3-GFP encoding plasmid (EndoA3+), treated with negative control siRNA (siCtrl) or with EndoA3-targeting siRNA (siEndoA3). Data are presented as fractions of WT siCtrl condition. The absolute concentration of secreted IFNγ in the supernatant of WT siCtrl condition is 2203 ± 201 (mean ± SEM) pg/mL.

F Quantification of IFNγ secretion (detected by ELISA) from CD8 T cells, cultured alone (T only) or co-cultured for 20h at 37°C with EndoA3+ LB33-MEL cells transfected with siRNAs: negative control (siCtrl), or against retromer subunits (siVPS35 or siVPS26A). Data are presented as fractions of siCtrl condition. The absolute concentration of secreted IFNγ in the supernatant of siCtrl condition is 4077 ± 99.62 (mean ± SEM) pg/mL. Quantification of VPS35 and VPS26A depletion is shown in Fig. S4B.

Data information: In (B-C), data are pooled from five independent experiments. In (E), data are pooled from six independent experiments. In (F), data are pooled from three independent experiments. In (E-F), data are presented as mean ± SEM. ns, not significant. *P < 0.05, **P < 0.01, ***P < 0.001 (B-C, paired *t* test; E, RM one-way ANOVA with Tukey's multiple comparison test; F, RM one-way ANOVA with Dunnett's multiple comparison test). Source data are available online for this figure.

cell activation. To further explore this possibility, we assessed the impact of disrupting the retromer complex in cancer cells on CD8 T cell activation. We depleted the retromer subunits VPS26A and VPS35 using RNA interference in LB33-MEL EndoA3+ cells, and then examined the effects on CD8 T cell activation by measuring IFNγ secretion. While VPS35 depletion had no significant effect, depleting VPS26A significantly impaired CD8 T cell activation (**Fig. 3F**, S4B).

In conclusion, these data demonstrate that EndoA3-dependent endocytosis in cancer cells enhances CD8 T cell activation, which correlates with an increase of the retrograde transport of immune synapse components, such as ALCAM and ICAM1. Depletion of the retromer component VPS26A inhibits CD8 T cell activation. Thus, blocking EndoA3-mediated CIE and subsequent retrograde transport likely prevents the efficient recruitment of ALCAM and ICAM1 components to the immune synapse, disrupting their polarized redistribution from the TGN.

Inhibition of EndoA3-dependent endocytosis and retrograde transport affects ICAM1 recruitment to the vicinity of CD8 T cells

Building on the data presented above, effective EndoA3-dependent endocytosis enhances CD8 T cell activation, possibly through an increased retrograde flux to the TGN and the subsequent polarized redistribution of immune synapse components to the plasma membrane. According to this hypothesis, depletion of EndoA3 or retromer subunits should perturb the recruitment of components to the immune synapse. Consequently, the structural features of the immune synapses would likely be affected. To test this, we monitored the recruitment of ICAM1 to the immune synapse using high resolution Airyscan confocal microscopy, given the well-established role of ICAM1 in T cell activation (40).

While we were able to transiently transfect LB33-MEL cells with an ICAM1-expressing plasmid (**Fig. 2B**), the transfection efficiency was low, thereby limiting the possibility of using LB33-MEL cells for immune synapse imaging. To overcome this, we generated a stable HLA-A*68012-expressing HeLa cell line. Wild-type HeLa cells lack HLA-A*68012 and are therefore unable to present the MUM-3 antigenic peptide to stimulate CD8 T cell activation (Fig. S5A). Upon addition of exogenous MUM-3 peptide, the HLA-A*68012-expressing HeLa cells successfully stimulated anti-MUM-3 CD8 T cells to secrete IFNγ (Fig. S5A) and proliferate (Fig. S5B). Thereby, these data confirmed the functionality of this HLA-A*68012-expressing HeLa cell line.

To monitor the recruitment of ICAM1 to the immune synapse, HLA-A*68012-expressing HeLa cells transiently expressing GFP-tagged ICAM1 were loaded with MUM-3 peptide and co-cultured with CD8 T cells. Using Airyscan live-cell imaging, we observed ICAM1-containing vesicular structures moving from inside the cells towards the contact area with CD8 T cells, where they seemed to fuse with the immune synapse-like conjugate (**Fig. 4A**, white arrowheads; Movie S6). In addition, immunofluorescence experiments using HeLa cells transiently expressing ICAM1-mScarlet revealed a strong accumulation of ICAM1 signal in the contact zone with CD8 T cells (Fig. S5C, white arrowheads).

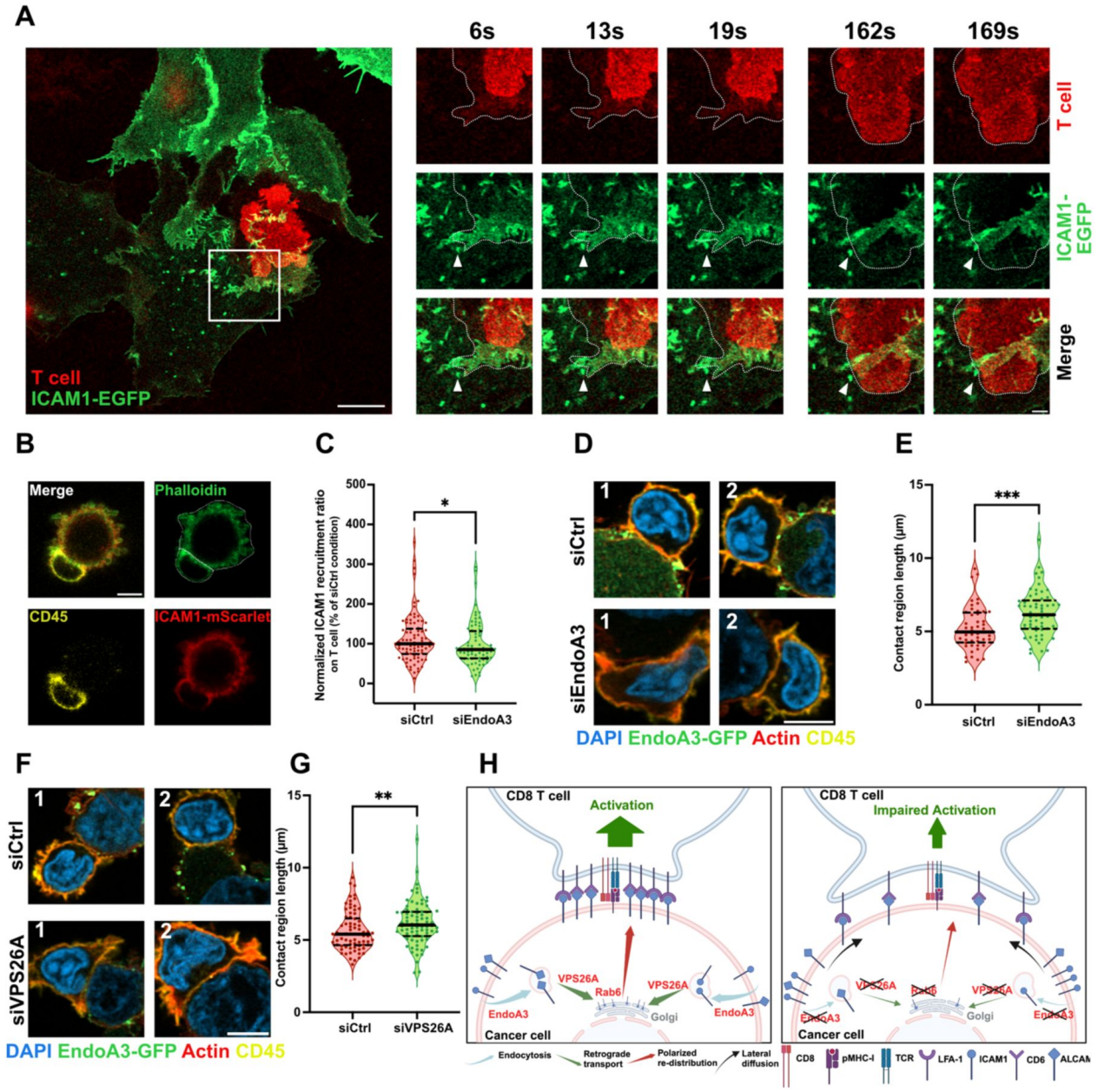
A
6s
13s
19s
162s
169s
T cell
ICAM1-EGFP
Merge
T cell
ICAM1-EGFP
B
Merge
Phalloidin
CD45
ICAM1-mScarlet
C
Normalized ICAM1 recruitment ratio on T cell (% of siCtrl condition)
*
siCtrl
siEndoA3
D
siCtrl
siEndoA3
DAPI EndoA3-GFP Actin CD45
E
Contact region length (μm)
***
siCtrl
siEndoA3
F
siCtrl
siVPS26A
DAPI EndoA3-GFP Actin CD45
G
Contact region length (μm)
**
siCtrl
siVPS26A
H
CD8 T cell
Activation
VPS26A
Rab6
EndoA3
Golgi
Cancer cell
CD8 T cell
Impaired Activation
Endocytosis
Retrograde transport
Polarized re-distribution
Lateral diffusion
CD8
pMHC-I
TCR
LFA-1
ICAM1
CD6

Figure 4.

Inhibition of EndoA3-mediated endocytosis and retrograde transport affects ICAM1 recruitment to and structure of immune synapses

A Live-cell Airyscan images of an immune synapse-like conjugate formed between a CD8 T cell (red) and an adherent stable HLA-A*68012-expressing HeLa cell line transiently expressing ICAM1-EGFP (green). Time series show enlarged cropped areas extracted from Movie S6. The dashed line contours delineate the contact area between the HeLa cell and the CD8 T cell. White arrowheads show two ICAM1-positive vesicular structures moving towards the contact area. Scale bars: 10 µm (full size image), 2 µm (enlarged cropped areas).

B Airyscan images of an immune synapse-like conjugate formed between a CD8 T cell (stained for CD45, yellow) and a stable HLA-A*68012-expressing HeLa cell (stained for actin, green) transiently expressing ICAM1-mScarlet (red) in suspension. Cell segmentation (white contour) was based on the actin staining for further quantifications (C). Scale bar: 5 µm.

C Quantification of relative ICAM1 recruitment to the vicinity of CD8 T cell when an immune synapse-like conjugate is formed between a CD8 T cell and a stable HLA-A*68012-expressing HeLa cell transiently expressing ICAM1-mScarlet in suspension. HLA-A*68012-expressing HeLa cells were transfected for 72h with siRNAs: negative control (siCtrl) or against EndoA3 (siEndoA3). Western blot analysis of EndoA3 depletion is shown in Fig. S5E. n conjuagates: siCtrl, n = 85; siEndoA3, n = 75.

D,F Airyscan images of immune synapse-like conjugates formed between CD8 T cells (stained for CD45, yellow) and stable EndoA3-GFP-expressing LB33-MEL cells (EndoA3-GFP, green) transfected for 72h with different siRNAs: negative control (siCtrl), siRNAs against EndoA3 (siEndoA3, D) or against VPS26A (siVPS26A, F). Actin (phalloidin, red) and nuclei (DAPI, blue) were also stained. Two examples are displayed per condition. Scale bar: 5 µm.

E,G Quantifications of the sizes of immune synapse-like conjugates formed between CD8 T cells and stable EndoA3-GFP-expressing LB33-MEL cells transfected with different siRNAs from images in panels D and F. Western blot analyses of EndoA3 and VPS26A depletion are shown in Fig. S6C and S6D. (E) n conjugates: siCtrl, n = 48; siEndoA3, n = 58. (G) n conjugates: siCtrl, n = 74; siVPS26A, n = 78.

H Working model. Immune synapse components ALCAM and ICAM1 are endocytosed into cancer cells through EndoA3-mediated CIE and are subsequently transported to the *TGN* in a retromer-dependent retrograde manner. Upon immune synapse formation, immune synapse components, such as ALCAM and ICAM1, are efficiently recruited to the contact area with CD8 T cells, likely from the *TGN* by polarized re-distribution, which can stabilize the immune synapse and promote CD8 T cell activation (left). Consequently, disruption of EndoA3-mediated CIE or retromer-dependent retrograde transport in cancer cells impair the efficient recruitment of immune synapse components to the contact area with CD8 T cells. In this situation, CD8 T cells expand their contact areas with cancer cells to try to compensate the loss of immune synapse components. The compensation is insufficient, which ultimately results in impaired T cell activation (right).

Data information: In (A), (B), (D) and (F), images are representative of three independent experiments. In (C), (E) and (G), data are pooled from three independent experiments. Data are presented as median and quartiles. *P < 0.05, **P < 0.01, ***P < 0.001 (C, Kolmogorov-Smirnov test; E and G, Mann-Whitney test). Source data are available online for this figure.

Next, we treated ICAM1-mScarlet-expressing HeLa cells with control or EndoA3 siRNAs and incubated them with CD8 T cells (**Fig. 4B-C**, S5D-E). To facilitate quantification, this experiment was conducted on cells in suspension, which adopt a regular spherical shape, making them easier to segment using quantification algorithms (**Fig. 4B**, S5D, phalloidin channel). We measured the ICAM1 recruitment ratio in the vicinity of T cells (see Materials and Methods). Surprisingly, the

ICAM1 signal was not confined to the contact region of the conjugates, but often extended around the entire T cell (**Fig. 4B**, S5D). Quantifications revealed that depletion of EndoA3 in HLA-A*68012-expressing HeLa cells caused a slight but significant decrease in ICAM1 recruitment to the vicinity of anti-MUM-3 CD8 T cells (**Fig. 4C**), consistent with the previously observed impaired T cell activation (**Fig. 3**).

We then explored the consequences of EndoA3 or VPS26A depletion in cancer cells on the morphology of immune synapses. To study this, we returned to the LB33-MEL EndoA3+ cell line and imaged immune synapses formed with the CD8 T cells using Airyscan confocal microscopy (**Fig. 4D** and **4F**, S6A-B). This experiment was also performed on cells in suspension for ease of quantitative analysis. We observed that immune synapses formed between CD8 T cells and EndoA3-depleted or VPS26A-depleted LB33-MEL EndoA3+ cells were larger than those formed between CD8 T cells and control LB33-MEL EndoA3+ cells. Quantification of immune synapse sizes confirmed this observation, showing that the immune synapses were 24% and 12% larger following EndoA3 and VPS26A depletion, respectively (**Fig. 4E** and **4G**). Of note, the efficiency of siRNA transfections was validated by Western blot (Fig. S6C-D).

Together, these results suggest that CD8 T cells attempt to compensate for the reduced recruitment of immune synapse components, caused by inhibition of CIE or retrograde transport in cancer cells, by enlarging the size of the immune synapses. However, despite their increased size, these immune synapses fail to effectively promote CD8 T cell activation (**Fig. 3** and S4).

In conclusion, disruption of endoA3-mediated CIE and subsequent retrograde transport in cancer cells impairs the recruitment of immune synapse components, such as ALCAM and ICAM1, likely by disrupting their polarized redistribution from the TGN to the plasma membrane for immune synapse formation with autologous CD8 T cells. As a result, this leads to decreased co-stimulatory signals, which are necessary for effective CD8 T cell activation. Although T cells try to compensate for the reduced co-stimulatory signals by expanding their contact area with cancer cells, this compensation is insufficient, ultimately impairing T cell activation (**Fig. 4H**).

Discussion

In this study, we discovered that ICAM1 is a new cargo of EndoA3-mediated CIE, expanding the list of known EndoA3-dependent cargoes, which previously included the Ig-like cell proteins ALCAM and L1CAM (26, 29). Interestingly, the first study by Boucrot *et al.* (2015) on Fast Endophilin-Mediated Endocytosis (FEME) did not report any effect on the internalization of ICAM1 when all the three EndoA isoforms were depleted. This discrepancy could be attributed to differences in the cell lines used. Boucrot *et al.* (2015) used a human T cell line (Kit255), in which EndoA3 might be poorly expressed (17, 53), while we used human cancer cell lines – HeLa cells with endogenous EndoA3 expression and the LB33-MEL melanoma cell line engineered to stably express EndoA3. Moreover, it is now widely accepted that FEME is primarily mediated by the EndoA2 isoform (2).

Notably, all three confirmed EndoA3-dependent endocytic cargoes – ALCAM, L1CAM and ICAM1 – are Ig-like cell adhesion molecules. This suggests the possibility of a common recognition pattern for EndoA3-mediated CIE. Unlike CME, where cargo recognition is typically mediated by adaptor protein binding to specific sorting signals in the cytosolic tails of the cargoes (54), the mechanisms for cargo recognition in CIE are just beginning to emerge (28, 55). In FEME, EndoA2 is thought to directly recognize and sort G protein-coupled receptors (GPCRs) by binding to PRDs in GPCRs through their SH3 domains (23, 56), or indirectly sort cargoes by interacting with other proteins, such as binding to CIN85 for EGFR and HGFR (57, 58), or srGAP1 for ROBO1 (59). However, how EndoA3-dependent endocytic cargoes are recognized and sorted remains unclear. Our lab has previously shown that the cytosolic tails of ALCAM and L1CAM

physically interact with EndoA3, but not with EndoA2 (26, 29). However, specific interaction motifs have not yet been identified in these two cargoes, and it remains uncertain whether the interaction with EndoA3 is direct or indirect. If direct, it is still unknown which part of EndoA3 mediates this interaction. Nevertheless, the accumulating evidence that Ig-like cell adhesion molecules are preferentially EndoA3-dependent cargoes suggests the existence of a shared recognition pattern within this cargo family, warranting further investigations.

In addition, we found that two of the three confirmed EndoA3-dependent endocytic cargoes, ALCAM and ICAM1, are also retrograde transport cargoes dependent on the retromer complex. The fact that ICAM1 follows a retromer-dependent retrograde transport route aligns with previous proteomic analyses of retromer-dependent cargoes, where ICAM1 was identified among the hits (60). While the link between retrograde transport and cell polarity has been well-established (9–11), the relationship between CIE and subsequent retrograde transport in polarized cellular contexts has largely been unexplored. Here, we propose that EndoA3-dependent cargoes, such as ICAM1 and ALCAM, use the retrograde transport route, thereby linking this specific CIE pathway to polarized cellular environments.

The retromer complex is one of the two complexes responsible for retrieving cargoes from endosomes for retrograde transport. The other complex, named Commander, consists of the CCC and retriever complexes. The CCC complex is made up of two coiled-coil domain-containing proteins CCDC22 and CCDC93, ten COMMD (copper metabolism MURR1 (Mouse U2af1-rs1 region 1) domain) family members COMMD1-COMMD10, and DENND10 (differentially expressed in normal and neoplastic cells-containing protein 10, also called FAM45A) (7, 61–63). The retriever complex, structurally similar to the retromer complex, is composed of C16orf62 (VPS35L), DSCR3 (VPS26C), and VPS29 (6, 64). Generally, the Commander complex is considered to be responsible for retromer-independent endosomal cargo sorting for retrograde transport, although many cargoes can utilize both complexes (6). Our study confirmed that both ALCAM and ICAM1 are retromer-dependent retrograde transport cargoes. However, while depletion of the retromer subunits VPS35 and VPS26A both impaired the retrograde transport of ALCAM and ICAM1 in HeLa cells, the effect of VPS26A depletion was consistently more pronounced than that caused by the loss of VPS35 (**Fig. 1C-D**). Moreover, only VPS26A depletion impaired CD8 T cell activation, while VPS35 depletion had no significant effect (**Fig. 3F**). Western blot analyses confirmed that VPS35 siRNA treatment led to a significant reduction in VPS26A levels, whereas VPS26A siRNA treatment resulted in a milder loss of VPS35 (**Fig. 1C-D**, S1C and S1E). This observation is in agreement with a previous report suggesting that VPS29 and VPS35 form a stable subcomplex *in vivo*, and that depletion of VPS35 or VPS29 leads to the degradation of other subunits, whereas VPS26A depletion has minimal effects on VPS29 and VPS35 levels (65).

Based on these observations, we hypothesize that there may be a mutual compensatory relationship between the retromer and Commander complexes for some cargoes. Depletion of VPS35 in HeLa cells causes an almost complete loss of the retromer complex, potentially triggering compensation by the Commander complex. However, VPS26A depletion preserves the VPS29-VPS35 intermediate of the retromer complex (65), which may inhibit compensation by the Commander complex through mechanisms that remain to be explored. This could explain why VPS35 depletion had a milder effect on the retrograde transport of ALCAM and ICAM1 (**Fig. 1C-D**) and why it did not significantly affect CD8 T cell activation (**Fig. 3F**). Future investigations on the potential mutual compensation between the retromer and Commander complexes in the retrograde transport of Ig-like proteins will be necessary.

In conclusion, this study identifies ICAM1 as a novel EndoA3-dependent endocytic cargo, alongside ALCAM, and demonstrates that both are retrograde transport cargoes dependent on the retromer complex. These cargoes are important components of immune synapses. Disruption of EndoA3-mediated endocytosis and retromer-dependent retrograde transport in cancer cells impairs CD8 T cell activation. Our data support the hypothesis that disruption of these trafficking pathways

prevents the efficient recruitment of immune synapse components via retrograde transport to the TGN, and subsequently their polarized redistribution to the plasma membrane. Our findings establish a connection between a well-defined CIE mechanism and a polarized cellular context through retrograde transport. Furthermore, our results may have implications for pathophysiological conditions where protein trafficking pathways can be modulated to enhance or inhibit immune recognition and tumor elimination. Targeting protein trafficking mechanisms as a therapeutic strategy appears as an exciting and tempting possibility that warrants further exploration in future studies.

Materials and methods

Cell culture

Wild-type HeLa cell line was from ATCC®. GalT-GFP-SNAP-expressing HeLa cell line was generated in a previous study (66). EndoA3-GFP-expressing HeLa cell line was previously generated by our lab (26). HLA-A*68012-expressing HeLa cell line was generated for the current study. Wild-type LB33-MEL cell line was derived from a melanoma patient in 1988 in de Duve Institute (45). EndoA3-GFP-expressing and GalT-GFP-SNAP-expressing LB33-MEL cell lines were generated for the current study. Anti-MUM-3 CD8 T cells were derived from the same melanoma patient in 1990 in de Duve Institute (45). Epstein-Barr virus transformed B cells from cancer patient LG-2 (LG-2 EBV) were obtained as described (67).

Wild-type HeLa cells were cultured at 37°C under 5% CO_2 in high glucose DMEM (Gibco, 41966-029) supplemented with 10% FBS (Dulis, 500105N1N), 100 U/mL penicillin and 100 µg/mL streptomycin (Penicillin-Streptomycin, Gibco, 15140-122). EndoA3-GFP-expressing, GalT-GFP-SNAP-expressing, and HLA-A*68012-expressing HeLa cells were cultured at 37°C under 5% CO_2 in high glucose DMEM (Gibco, 41966-029) supplemented with 10% FBS, 100 U/mL penicillin, 100 µg/mL streptomycin, and 0.5 mg/mL G418 (Roche, 108321-42-2). WT LB33-MEL cells were cultured at 37°C under 5% CO_2 in IMDM (Gibco, 12440-053) supplemented with 10% FBS, 100 U/mL penicillin, 100 µg/mL streptomycin, 1.5 mM GlutaMAX I (Gibco, 35050-038), and 0.05 mM β-mercaptoethanol (Gibco, 21985-023). Empty plasmid stably transfected (Φ), EndoA3-GFP-expressing, and GalT-GFP-SNAP-expressing LB33-MEL cells were cultured in the same medium as WT LB33-MEL cells but supplemented with 0.7 mg/mL G418 (Roche, 108321-42-2). Anti-MUM-3 CD8 T cells were freshly thawed from cryovials and cultured at 37°C under 5% CO_2 in IMDM (Gibco, 12440-053) supplemented with 10% HS (Ludwig Institute for Cancer Research (LICR), Brussels Branch), 100 U/mL penicillin, 100 µg/mL streptomycin, 1.5 mM GlutaMAX I, and extra 5 U/mL DNase I (STEMCELL Technologies, 07469) and 50 U/mL IL-2 (PROLEUKIN®, CNK 1185-958) for at least 4 h before usage. For culture, T cells were maintained with the same medium, but without DNase I. LG-2 EBV cells were cultured at 37°C under 8% CO_2 in IMDM (Gibco, 21980-032) supplemented with 10% FBS (Gibco, A5256701), 100 U/mL penicillin, 100 µg/mL streptomycin and 1.5 mM GlutaMAX I (Gibco, 35050-038).

DNA constructs and transfection

Plasmids used in this study are listed below:

Protein	Backbone	Tag	Source
EndoA3	pIRESneo2	GFP	F. Tyckaert, LIBST, BE
/	pIRESneo3	/	Clontech
ICAM1	pLV-mScarlet	mScarlet	J. D. Van Buul, Amsterdam UMC, NL
ICAM1	pEGFP-N1	EGFP	Generated in the lab for this study
GalT-GFP-SNAP	pSNAP-tag	GFP	L. Johannes, Institut Curie, FR
/	pEGFP-N1	EGFP	Clontech
HLA-A*68012	pcDNA3	/	P. van der Bruggen, de Duve Institute, BE

C-terminally EGFP-tagged ICAM1 expression plasmid was generated in the current study for live-cell imaging. ICAM1 sequence was first amplified by PCR from the aforementioned mScarlet-tagged ICAM1 expression plasmid, and then inserted into the pEGFP-N1 vector by Gibson Assembly® (New England Biolabs). To do so, the vector was linearized with the restriction enzyme EcoR I, and corresponding overlapping sequences were added to both ends of ICAM1 inserts by PCR (forward primer: 5'-CGAGCTCAAGCTTCGATGGCTCCCAGCAGC-3'; reverse primer: 5'-TACCGTCGACTGCAGGGGAGGCGTGGCTTG-3'). The Gibson assembly product was then amplified in *E. coli* DH10B strain and validated by sequencing.

For immunofluorescence and live-cell imaging experiments, plasmids were transfected with FuGene HD (Promega), according to the manufacturer's instructions. Cells were used for experiments 16–24 h after transfection.

To generate the stable HLA-A*68012-expressing HeLa cell line, the pcDNA3-HLA-A*68012 plasmid was transfected into wild-type HeLa cells by nucleofection (Amaxa Nucleofector 2b, Lonza) according to the built-in protocol. Transfected cells were cultured for 2 days. A selection pressure was then imposed by supplementing the culture medium with 1 mg/mL G418 for 7 days. Cells were then harvested and maintained with 0.5 mg/mL G418 in the culture medium.

For the generation of different stable LB33-MEL cell lines, 300,000 wild-type LB33-MEL cells were seeded in 2 mL culture medium. 4 µg of corresponding plasmid (pIRESneo3 for LB33-MEL Φ generation, pIRESneo2-EndoA3-GFP-FKBP for EndoA3-GFP-expressing LB33-MEL generation, and pGalT-GFP-SNAP-tag for GalT-GFP-SNAP-expressing LB33-MEL generation) were added to 200 µL of Opti-MEM (Gibco), followed by addition of 24 µL of FuGENE HD (Promega) and gentle mixing. The mix was incubated for 15 min at room temperature, and then added to the cells. After 2 days of culture, transfected cells were selected by supplementing the culture medium with 0.7 mg/mL G418 for 7-15 days. Cell sorting based on GFP fluorescence was then conducted with the FACSAria flow cytometer (BD Biosciences) to yield a 100% positive stable EndoA3-GFP-expressing LB33-MEL cell line. For LB33-MEL cells transfected with GalT-GFP-SNAP-expressing plasmid, the homogeneity of cells was checked on a FACSVerse at the end of selection, and all cells were GFP-positive. Stable LB33-MEL Φ, EndoA3-GFP-expressing LB33-MEL and GalT-GFP-SNAP-expressing LB33-MEL cell lines were then maintained with continuous presence of 0.7 mg/mL G418 in the culture medium.

RNA interference

siRNAs were used to knock down target molecules in HeLa and LB33-MEL cell lines at a total final concentration of 40nM. For HeLa cells, 150,000 cells were seeded per well of a 6-well plate for each siRNA condition, and siRNA transfection was conducted with 1 µL Lipofectamine RNAiMAX (ThermoFisher). For LB33-MEL cells, 200,000 cells were seeded per well of a 6-well plate for each siRNA condition, and siRNA transfection was conducted with 2 µL Lipofectamine RNAiMAX (ThermoFisher). All experiments were done 72 h after siRNA transfection. All siRNAs were purchased from QIAGEN, and their sequences are listed as follows:

Name	Reference	Sequence
Hs_SH3GL3_5	SI04170376	CCAGACGAGAATACAAGCCAA
Hs_SH3GL3_6	SI04176529	CCAGACGAAGAAGTCAGACAA
Hs_VPS26A_1	SI03122273	AAAGGTAAACCTAGCCTTTAA
Hs_VPS26A_2	SI04197914	TGCCACCTATCCTGATGTTAA
Hs_VPS35_7	SI04287605	CAGAATTGCCCTTAAGACTTT
Hs_VPS35_8	SI04316914	TTGCTGCATCCAAACTTCTAA
Rab6 HP Custom siRNA	NA	AAGACAUCUUUGAUCACCAGA
AllStars Negative Control	SI03650318	NA

T cell proliferation assay

HLA-A*68012 expressing HeLa cells were detached with PBS-EDTA 2 mM and resuspended to 1,000,000 cells/mL in the culture medium supplemented with or without MUM-3 peptide (EAFIQPITR) at 300 ng/mL. Then, HeLa cells and LG-2 EBV feeder cells were γ-irradiated for 45min (100Gy), washed, and maintained in T cell culture medium until the initiation of co-culture with T cells. The anti-MUM-3 CD8 T cells were thawed the day before and were harvested, washed, and resuspended in complete T cell culture medium with 0.5 µM CMFDA (Invitrogen™, C2925) for 20 min at 37°C. T cells were then washed and resuspended to 300,000 cells/mL in T cell medium supplemented with 50 U/mL IL-2. In an ultra-low attachment round bottom 96-well plate (Corning® Costar®, CLS7007), 30,000 anti-MUM-3 CD8 T cells were seeded with 10,000 HeLa cells and 90,000 γ-irradiated LG-2 EBV feeder cells. The plate was quickly centrifuged and then incubated for 4 days at 37°C with 5% CO_2. Cells were then transferred on ice for antibody staining and flow cytometry analysis.

Flow cytometry data were acquired with a LSR Fortessa (BD Biosciences) and were analyzed using FlowJo (v10.8.1) software.

IFNγ secretion assay

CD8 T cells were thawed and cultured as described above. siRNA transfected LB33-MEL cells were harvested 72 h after the siRNA transfection and were resuspended to 300,000 cells/mL in T cell medium. CD8 T cells were then washed and resuspended to 300,000 cells/mL in fresh T cell medium supplemented with 50 U/mL IL-2. 100 µL of LB33-MEL cells and 100 µL of T cells were pooled together in a 96-well plate and were co-cultured for 20 h at 37°C under 5% CO_2. A technical triplicate was made for each siRNA condition. The supernatant was collected the next day for ELISA analysis.

ELISA plate was coated with 50 µL IFNγ monoclonal coating antibody solution (Invitrogen, AHC4432; 1:250 dilution in PBS) in each well and was incubated at 4°C overnight. On the next day, two standard IFNγ concentration ladders were prepared: 1:2 dilutions for 7 successive times with T cell medium in 96-well plate (original concentration of 10,000 pg/mL; the last well contains only medium). The ELISA plate was washed with washing buffer (0.154 M NaCl solution with 0.1% Tween-20) twice and with water once to remove unbound antibody. 50 µL of supernatant and standard IFNγ ladders were then added to the ELISA plate, followed by the addition of 50 µL IFNγ monoclonal detecting antibody solution (biotin conjugated; Invitrogen, AHC4539; 1:1000 dilution in T cell medium) into each well. The plate was incubated on a shaker at 37°C for 2 h, and then was washed again. 50 µL of Streptavidin-Peroxydase solution (Sigma, S5512; 1:1000 dilution in PBS containing 0.5% bovine serum albumin) was added to each well and the plate was again incubated at 37°C for 30 min. Then, the plate was washed and 100 µL of 1-Step Ultra TMB-ELISA Substrate Solution (ThermoFisher, 34028) was added to each well. When the blue color of TMB stopped getting darker, 20 µL of sulfuric acid (1 M) was added to each well to stop the reaction (the blue color turned yellow). The absorbance of substrate solution at 450 nm was then measured with an ELISA Analyzer (Bio-Rad Microplate Reader) and the IFNγ concentration was determined.

Quantification of intracellular cytokines in CD8 T cells

CD8 T cells were thawed and cultured as described above. LB33-MEL cells were harvested 72 h after siRNA transfection and resuspended to 100,000 cells/mL in T cell medium. T cells were then washed and resuspended to 100,000 cells/mL in fresh T cell medium supplemented with 50 U/mL IL-2. 100 µL LB33-MEL cells and 100 µL T cells were pooled together in a 96-well “U” bottom plate and were co-cultured at 37°C under 5% CO_2 for 1 h. Then, Brefeldin A (Sigma, B7651-5MG) was added to each well at a final concentration of 5 µg/mL. Co-culture continued for another 3 h, after which cells were transferred to a 96-well “V” bottom plate and washed with 150 µL/well of staining

buffer (PBS with 1mM EDTA and 1% HS). The plate was quickly spun at 400×g for 3 min and supernatant was removed. 50 µL of extracellular staining antibody solution for CD8 and viability marker prepared with staining buffer were added to each well and mixed. The plate was then maintained at 4°C for 20 min in the dark. Afterwards, cells were washed with 150 µL/well PBS and resuspended in 100 µL/well of 1% paraformaldehyde (PFA) for 10 min at room temperature. Cells were then washed with PBS again and resuspended in 100 µL PBS containing 1 mM EDTA, 1% HS, and 0.1% saponin. After 10 min incubation at room temperature, cells were centrifuged, and supernatant was removed. 50 µL of intracellular staining antibody solution for cytokines prepared with the same buffer was added to each well, and the plate was incubated in the dark for 30 min at room temperature. Finally, cells were washed and resuspended in 250 µL 1% PFA for flow cytometry analysis.

Flow cytometry data were acquired with a FACSVerse (BD Biosciences) and were analyzed using FlowJo (v10.8.1) software.

Western blotting

Cell lysates were prepared with 200,000 cells and 50 µL of sample buffer (62.5 mM Tris-HCl pH 6.8, 2% sodium dodecyl sulfate (SDS), 5% glycerol, 2.5% β-mercaptoethanol, 0.005% blue bromophenol). Lysate samples were boiled at 95°C for 10 min before loading onto 4–15% Mini-PROTEAN® TGX™ precast protein gels (Bio-Rad, 4561084), as well as prestained protein standard. For the SNAP-Tag-based retrograde transport assay (see below), HiMark™ Pre-stained Protein Standard (Invitrogen, LC5699) was used; for all the other western blots, Broad Range (10-250 kDa) Color Prestained Protein Standard (New England Biolabs, P7719S) was used. After electrophoresis, proteins were transferred onto a PVDF membrane (pre-activated with methanol for 1 min; Millipore, IPFL85R) using a wet transferring system. The membrane was then blocked in 5%-milk PBS-T (phosphate-buffered saline, 0.1% Tween-20) for 1h at room temperature, then stirred overnight at 4°C with primary antibody in the same solution. The next day, the membrane was incubated with corresponding horseradish peroxidase (HRP) conjugated secondary antibodies for 1h at room temperature. Chemiluminescent (ECL) substrate (SuperSignal™ West Femto Maximum Sensitivity Substrate, ThermoFisher, 34096, or SuperSignal™ West Pico PLUS Chemiluminescent Substrate, ThermoFisher, 34580) was used for image exposure with an Amersham ImageQuant™ 800 machine (Cytiva). Images were processed and quantified with ImageJ v2.14.0/1.54f (NIH) software.

SNAP-Tag-based retrograde transport assay

First, anti-ALCAM (Bio-Rad, MCA1926) and anti-ICAM1 (Bio-Rad, MCA1615) antibodies were labeled with benzylguanine (BG) by incubating them overnight at 4°C with a threefold molar excess of BG-GLA-NHS reagent (New England Biolabs, S9151S; prepared in anhydrous DMSO). The reaction was neutralized with 20 mM Tris (pH 7.4) for 10 min at 21°C. Free BG-GLA-NHS was eliminated by applying labelled antibodies on spin desalting columns with a 7 kDa cutoff (ThermoFisher, 89849), according to manufacturer's instructions. Then, retrograde transport assays were conducted according to previously published protocols (44).

Colocalization and uptake experiments

LB33-MEL cells were cultured on coverslips in 4-well plates to reach sub-confluence on the day of the experiment. Cells were pre-incubated in fresh serum-containing medium for 30 min at 37°C just before the experiment, then were incubated with anti-ALCAM antibody (Biolegend, 343902)-containing pre-warmed medium (5 µg/mL) for 15 min at 37°C to allow for endocytosis. For colocalization experiments, cells were quickly washed at 37°C with pre-warmed PBS and were subsequently fixed with pre-warmed 4% PFA for 20 min at 37°C in order to preserve the integrity of cellular structures and protein distribution. For uptake experiments, endocytosis was stopped on ice, and unbound antibodies were removed by extensive washes with ice-cold PBS++ (PBS

supplemented with 0.4 mM $MgCl_2$ and 0.9 mM $CaCl_2$). Residual cell surface-accessible anti-ALCAM antibodies were stripped by two 5 s acid washes on ice (200 mM acetic acid, pH 2.5, 300 mM NaCl, 5 mM NaCl, 1 mM $CaCl_2$, and 1 mM $MgCl_2$). After neutralization by extensive washes with ice-cold PBS++, cells were fixed with 4% PFA for 10 min on ice, followed by another 10 min at room temperature. For both experiments, after quenching with 50 mM NH_4Cl for at least 5 min, cells were permeabilized with 0.02% saponin in PBS containing 0.2% bovine serum albumin for 30 min at room temperature. After incubation with secondary antibodies in the same permeabilization solution for 30 min, samples were mounted with Fluoromount G (Invitrogen). Images were taken with a Zeiss LSM900 microscope equipped with an Airyscan detector and a Plan Apo 63× numerical aperture (NA) 1.4 oil immersion objective. For colocalization experiments, Airyscan mode was applied. Pixel size: 0.04 micron. For uptake experiments, confocal mode was used. Pixel size: 0.07 micron. Microscope software: Zen blue (v3.3; Zeiss).

Conjugate formation for confocal fixed sample imaging

For conjugate formation between adherent HLA-A*68012-expressing HeLa cells and anti-MUM-3 CD8 T cells (Fig. S5C), HeLa cells were cultured on coverslips and transiently transfected with ICAM1-mScarlet expression plasmid 16-24h before the experiment. HeLa cells were first incubated in 300 ng/mL MUM-3 peptide-containing culture medium for 45 min at 37°C and were then washed extensively with T cell culture medium to remove residual unbound peptide. T cells were freshly thawed as described above and resuspended to 500,000 cells/mL with T cell culture medium supplemented with 50 U/mL IL-2. Then, 250,000 T cells were added to HeLa cells and the pool was incubated for 20 min at 37°C. Cells were then fixed at room temperature for 20 min by adding PFA directly to the culture medium to reach a final concentration of 4%.

For conjugate formation between suspended HLA-A*68012-expressing HeLa cells and anti-MUM-3 CD8 T cells (**Fig. 4B**, S5D), HeLa cells were cultured in 6-well plates and transfected with negative control siRNAs or siRNAs targeting EndoA3 72h in advance and with plasmid expressing ICAM1-mScarlet 16-24h in advance. HeLa cells were detached with PBS-EDTA 4 mM, resuspended to 1,000,000 cells/mL in culture medium containing 300 ng/mL MUM-3 peptide and incubated for 45 min at room temperature. Then, HeLa cells were extensively washed with T cell culture medium, and finally resuspended to 1,000,000 cells/mL with T cell culture medium supplemented with 50 U/mL IL-2. T cells were freshly thawed as described above and resuspended to 1,000,000 cells/mL with T cell culture medium supplemented with 50 U/mL IL-2. Subsequently, 250,000 HeLa cells and 250,000 T cells were pooled together and further co-cultured on coverslips for 20 min at 37°C. Of note, coverslips were pre-coated with poly-L-lysine (Sigma-Aldrich, P4832) according to manufacturer's instructions to stabilize conjugates. Cells were then fixed at room temperature for 20 min by adding PFA directly to the culture medium to reach a final concentration of 4%.

For conjugate formation between suspended LB33-MEL EndoA3+ cells and anti-MUM-3 CD8 T cells (**Fig. 4D** and **4F**, S6A-B), LB33-MEL cells were transfected with negative control siRNAs or siRNAs targeting EndoA3 or VPS26A 72h in advance. LB33-MEL cells were detached with 0.05% Trypsin-EDTA (Gibco, 25300-054) and resuspended to 1,000,000 cells/mL with T cell culture medium supplemented with 50 U/mL IL-2. T cells were freshly thawed as described above and resuspended to 1,000,000 cells/mL with T cell culture medium supplemented with 50 U/mL IL-2. Then, 250,000 LB33-MEL cells and 250,000 T cells were pooled together and were co-cultured on poly-L-lysine pre-coated coverslips for 20 min at 37°C. Cells were then fixed at room temperature for 20 min by adding PFA directly to the culture medium to reach a final concentration of 4%.

After fixation with PFA and quenching with 50 mM NH_4Cl for at least 5 min, cells were permeabilized with 0.02% saponin in PBS containing 0.2% bovine serum albumin for 30 min, both at room temperature. Then, cells were successively incubated with primary and secondary antibodies in the same PBS-saponin solution for 30 min and mounted with Fluoromount G (Invitrogen). Images were taken with Zeiss LSM900 microscope equipped with an Airyscan detector and a Plan Apo 63× numerical aperture (NA) 1.4 oil immersion objective. For the ICAM1

recruitment experiment (Fig. S5C) and immune synapse morphology experiment (**Fig. 4D** and **4F**, S6A-B), z-stack was used. z-stack interval: 0.15 micron. For all images, Airyscan mode was applied. Pixel size: 0.04 micron. Microscope software: Zen blue (v3.3; Zeiss).

Conjugate formation for confocal live-cell imaging

HLA-A*68012-expressing HeLa cells were seeded in 24-well glass bottom plates (Greiner, 662892) and transfected with ICAM1-EGFP expression plasmid 16-24 h in advance. HeLa cells were first incubated in MUM-3 peptide-containing (300 ng/mL) culture medium for 45 min at 37°C and then washed extensively with T cell culture medium to remove residual unbound peptide. Anti-MUM-3 CD8 T cells were freshly thawed as described above and stained with Orange CellMask™ Plasma Membrane Stain (Invitrogen, C10045; 1:1000 dilution in T cell culture medium) for 10 min at 37°C, washed with culture medium, and resuspended to 500,000 cells/mL in T cell culture medium supplemented with 50 U/mL IL-2. 250,000 T cells were added to each well containing HeLa cells and live-cell imaging was started immediately after. Live-cell imaging was performed at 5% CO_2 and 37°C on a Zeiss LSM900 confocal microscope equipped with an Airyscan detector, an α Plan Apo 63× numerical aperture (NA) 1.4 oil immersion objective and a stage-top incubator. Microscope was controlled by software Zen blue (v3.3; Zeiss). Laser focus was maintained with definite focus 2. Airyscan mode was applied. Time interval between each frame: 6.5 s. Pixel size: 0.04 micron.

TIRF live-cell imaging

EndoA3-GFP-expressing HeLa/LB33-MEL cells were cultured on a 35 mm imaging dish with a glass bottom and low walls (ibidi, µ-Dish 35 mm, low, 80137) and transfected with ICAM1-mScarlet expression plasmid 16-24 h in advance. Live-cell imaging was conducted under 5% CO_2 and 37°C with Zeiss Axio Observer 7 microscope equipped with an iLas azimuthal TIRF module (Gattaca Systems), an α Plan-Apo 100× NA 1.46 oil immersion objective, an sCMOS Prime BSI Express camera (Photometrics) and a stage-top incubator (Tokai Hit). Microscope was controlled by Metamorph® software (v7.10.4.407; Molecular Devices). Laser focus was maintained with definite focus 3. Time interval between each frame: 1 s. Pixel size: 0.065 micron.

Microscope image analyses and quantifications

Airyscan image processing was performed with Zen blue (v3.3; Zeiss). Images were quantified with (Fiji Is Just) ImageJ v2.14.0/1.54f (NIH) software as follows.

For CD166 uptake experiments, images were quantified using Icy v2.4.2.0 (Institut Pasteur) software. Briefly, regions of interest (ROIs) were drawn manually around each cell. Within each ROI, bright spots corresponding to endocytic structures were automatically detected over dark background using the “Spot Detector” plugin. The plugin performs image denoising by computing wavelet adaptive threshold (WAT) on the union of all ROIs present in an image. This automatic thresholding was then manually adjusted, depending on the size of the spots. For each independent experiment, scale 2 was chosen and sensitivity was adjusted empirically. In addition, a size filter was added to discard spots smaller than 2 pixels. After processing, an excel file containing the fluorescence intensity of each endocytic structure was generated. The sum intensity of endocytic structures in each cell was calculated, then data were first adjusted according to the surface level of CD166 detected by flow cytometry in each experimental condition and were finally normalized to the control condition (set as 100%) for statistical analysis.

For conjugate formation experiments with HeLa cells to detect ICAM1 recruitment to the vicinity of CD8 T cells, masks were automatically generated for each image according to phalloidin staining by using Cellpose v3.0.7 software (68). First, an RGB format 512 × 512-pixel image of the phalloidin channel was generated from Fiji (ImageJ v2.14.0/1.54f) for each image and was imported to Cellpose. Segmentation of each cell was automatically performed using “cyto3” model

with diameter (pixels) set as 40 for all independent repeats and was then exported as a mask. The mask was then imported into Fiji and re-scaled to the real size of the original image. Wand tool was used to select ROI corresponding to single cells. In each ROI, the raw integrated density (RawIntDen) of ICAM1 signal was measured. Then, the ICAM1 recruitment ratio in the vicinity of the T cell was calculated as the ratio between the ICAM1 signal in the T cell ROI and the total ICAM1 signal in the ROIs of the T cell and the adjacent HeLa cell: "RawIntDen of ICAM1 signal in T cell ROI/(RawIntDen of ICAM1 signal in T cell ROI + RawIntDen of ICAM1 signal in HeLa cell ROI)". Data were normalized to control condition (set as 100%) for each independent repeat and were then pooled together for statistical analysis.

For conjugate formation experiments to measure the size of immune synapses, z-stack images (z-stack interval: 0.15 micron) for each conjugate were imported to Fiji. The contact region between a CD8 T cell and an LB33-MEL cell was delineated by "freehand line" tool manually, and then the length of the line was measured for each z-stack. The largest value was picked out from all z-stacks and was considered as the size of this immune synapse. All data from three independent repeats were then pooled together for statistical analysis.

Statistical analyses

Statistical analyses were performed with GraphPad Prism v10.1.0. D'Agostino–Pearson omnibus normality test was used to check the normality of datasets. If data passed the normality test, parametric tests were used, and data were plotted on graphs as mean ± SEM as error bars. If data did not pass the normality test, nonparametric tests were used, and data were plotted on graphs as median and quartiles. Details on the parametric and nonparametric tests used for each analysis are indicated in figure legends. Significance of comparison is represented on the graphs by asterisks.

Antibodies and reagents

Product	Reference	Application	Dilution
PE anti-human CD166 antibody	Biolegend, 343904	FACS	1:1000
APC anti-human CD54 antibody	BD Pharmingen, 561899	FACS	1:60
APC anti-HLA-A2, A28 antibody	Miltenyi Biotec, 130-099-582	FACS	1:300
Viability Dye eFluor 780	Invitrogen, 65-0865-14	FACS	1:1000
PerCP-Cy5.5 anti-human CD8 antibody	BD Pharmingen, 624060	FACS	1:100
APC anti-human IL-2 antibody	Biolegend, 500310	FACS	1:25
BV421 anti-human TNF-α antibody	Biolegend, 502932	FACS	1:100
PE anti-human IFNγ antibody	BD Pharmingen, 554701	FACS	1:200
Biotin anti-human HLA-A2 Antibody	Biolegend, 343322	FACS	1:400
CMFDA	Invitrogen, C2925	FACS	0.5 μM
Anti-IFNγ coating antibody	Invitrogen, AHC4432	ELISA	1:250
Biotin anti-IFNγ detecting antibody	Invitrogen, AHC4539	ELISA	1:1000
Streptavidin−Peroxidase	Sigma-Aldrich, S5512	ELISA	1:1000
1-Step Ultra TMB-ELISA Substrate	ThermoFisher, 34028	ELISA	100 μL
Anti-SH3GL3/Endophilin-A3 antibody	Sigma-Aldrich, HPA039381	WB	1:1000
Anti-α-tubulin antibody	Sigma-Aldrich, T5168	WB	1:10000
Anti-VPS26A antibody	abcam, ab23892	WB	1:1000
Anti-VPS35 antibody	abcam, ab10099	WB	1:500
HRP conjugated anti-mouse antibody	Agilent Technologies, P044701-2	WB	1:5000
HRP conjugated anti-rabbit antibody	Agilent Technologies, P044801-2	WB	1:5000

HRP conjugated anti-goat antibody	Santa Cruz Biotechnology, sc-2354	WB	1:1000
Anti-SNAP-tag® antibody	New England Biolabs, P9310S	WB	1:1000
Anti-Rab6 antibody	Abcam, ab95954	WB	1:1000
Anti-CD166 antibody	Bio-Rad, MCA1926	SNAP-Tag	10 µg/mL
Anti-CD54 antibody	Bio-Rad, MCA1615	SNAP-Tag	10 µg/mL
SNAP-Cell® Block	New England Biolabs, S9106S	SNAP-Tag	1:200
Anti-CD166 antibody	Biolegend, 343902	IF	1:100
Anti-CD45 antibody	Santa Cruz Biotechnology, sc-1178	IF	1:100
SNAP-Cell® TMR-Star	New England Biolabs, S9105S	IF	1:200
Anti-GM130 antibody	Biolegend, 937002	IF	1:200
Alexa Fluor™ 488 Phalloidin	Invitrogen, A12379	IF	1:200
Alexa Fluor™ 568 Phalloidin	Invitrogen, A12380	IF	1:200
Alexa Fluor™ 488 anti-Rabbit IgG	Invitrogen, A11008	IF	1:200
Alexa Fluor™ 568 anti-Mouse IgG	Invitrogen, A11031	IF	1:200
Alexa Fluor™ 633 anti-Mouse IgG	Invitrogen, A21050	IF	1:200
CellMask™ Plasma Membrane Stain	Invitrogen, C10045	IF	1:1000
DAPI	Sigma-Aldrich, D9542	IF	1:10000
Poly-L-lysine	Sigma-Aldrich, P4832	IF	NA

Acknowledgements

We thank J.D. van Buul (Amsterdam UMC, Netherlands) for kindly providing aforementioned plasmid. We thank E. Rigaux, F. Tyckaert, C. Wildmann, C. Duhamel, S. Meurant, A. Fattaccioli, S. Burteau and C. Demazy for their support and technical help in experiments. We thank E. Macdonald for proofreading the manuscript. We greatly thank Morph-Im platform of UNamur and flow cytometry & cell sorting platform (CYTF) from de Duve Institute of UCLouvain for giving access to advanced microscopy and flow cytometry technologies, respectively. S.X. is supported by a PhD fellowship from FSR (Fond Spécial de Recherche) of UNamur and UCLouvain. T.H. is a postdoctoral research fellow of the Fonds de la Recherche Scientifique (FNRS, Belgium). L.J. is supported by Mizutani Foundation for Glycosciences (reference n° 200014), Agence National de la Recherche (ANR-20-CE15-0009-01, ANR-22-CE11-0030-03, France), Fondation pour la Recherche Médicale (EQU202103012926, France) and an ERC Proof of Concept (project 101062030). P.V.D.B. and T.H. were supported by de Duve Institute (Belgium) and Université Catholique de Louvain (Belgium). P.M. is supported by a PDR (T.0163.21) and CDR (J.0127.23) from the Fonds de la Recherche Scientifique (FNRS, Belgium). H.-F.R. is supported by a Start-Up Grant Collen-Francqui from Francqui Foundation (Belgium), an Incentive Grant for Scientific Research (MIS-F.4540.21) and a Research Credit (CDR-J.0176.24) from the Fonds de la Recherche Scientifique (FNRS, Belgium), and a research grant from NARILIS institute (UNamur).

Additional files

Supporting information.

Movie S1.

Movie S2.

Movie S3.

Movie S4.

Movie S5.

Movie S6.

References

1. Kaksonen M., Roux A. 2018) **Mechanisms of clathrin-mediated endocytosis** *Nat Rev Mol Cell Biol* **19**:313–326

2. Renard H. F., Boucrot E. 2021) **Unconventional endocytic mechanisms** *Curr Opin Cell Biol* **71**:120–129

3. Sonnichsen B., De Renzis S., Nielsen E., Rietdorf J., Zerial M. 2000) **Distinct membrane domains on endosomes in the recycling pathway visualized by multicolor imaging of Rab4, Rab5, and Rab11** *J Cell Biol* **149**:901–914

4. van der Sluijs P., et al. 1992) **The small GTP-binding protein rab4 controls an early sorting event on the endocytic pathway** *Cell* **70**:729–740

5. Seaman M. N. 2004) **Cargo-selective endosomal sorting for retrieval to the Golgi requires retromer** *J Cell Biol* **165**:111–122

6. McNally K. E., et al. 2017) **Retriever is a multiprotein complex for retromer-independent endosomal cargo recycling** *Nat Cell Biol* **19**:1214–1225

7. Healy M. D., et al. 2023) **Structure of the endosomal Commander complex linked to Ritscher-Schinzel syndrome** *Cell* **186**:2219–2237

8. Seaman M. N., McCaffery J. M., Emr S. D. 1998) **A membrane coat complex essential for endosome-to-Golgi retrograde transport in yeast** *J Cell Biol* **142**:665–681

9. Shafaq-Zadah M., Dransart E., Johannes L. 2020) **Clathrin-independent endocytosis, retrograde trafficking, and cell polarity** *Curr Opin Cell Biol* **65**:112–121

10. Shafaq-Zadah M., et al. 2016) **Persistent cell migration and adhesion rely on retrograde transport of beta(1) integrin** *Nat Cell Biol* **18**:54–64

11. Carpier J. M., et al. 2018) **Rab6-dependent retrograde traffic of LAT controls immune synapse formation and T cell activation** *J Exp Med* **215**:1245–1265

12. Dieckmann N. M., Frazer G. L., Asano Y., Stinchcombe J. C., Griffiths G. M. 2016) **The cytotoxic T lymphocyte immune synapse at a glance** *J Cell Sci* **129**:2881–2886

13. Peter B. J., et al. 2004) **BAR Domains as Sensors of Membrane Curvature: The Amphiphysin BAR Structure** *Science* **303**

14. Gallop J. L., et al. 2006) **Mechanism of endophilin N-BAR domain-mediated membrane curvature** *EMBO J* **25**:2898–2910

15. Sparks A. B., Hoffman N. G., McConnell S. J., Fowlkes D. M., Kay B. K. 1996) **Cloning of ligand targets: systematic isolation of SH3 domain-containing proteins** *Nat Biotechnol* **14**:741–744

16. Micheva K. D., Kay B. K., McPherson P. S. 1997) **Synaptojanin forms two separate complexes in the nerve terminal. Interactions with endophilin and amphiphysin** *J Biol Chem*

272:27239–27245

17. Giachino C., et al. 1997) **A novel SH3-containing human gene family preferentially expressed in the central nervous system** *Genomics* **41**:427–434

18. So C. W., et al. 2000) **Expression and protein-binding studies of the EEN gene family, new interacting partners for dynamin, synaptojanin and huntingtin proteins** *Biochem J* **348**:447–458

19. Ringstad N., Nemoto Y., De Camilli P. 1997) **The SH3p4/Sh3p8/SH3p13 protein family: binding partners for synaptojanin and dynamin via a Grb2-like Src homology 3 domain** *Proc Natl Acad Sci U S A* **94**:8569–8574

20. Simpson F., et al. 1999) **SH3-domain-containing proteins function at distinct steps in clathrin-coated vesicle formation** *Nat Cell Biol* **1**:119–124

21. Gad H., et al. 2000) **Fission and Uncoating of Synaptic Clathrin-Coated Vesicles Are Perturbed by Disruption of Interactions with the SH3 Domain of Endophilin** *Neuron* **27**:301–312

22. Milosevic I., et al. 2011) **Recruitment of endophilin to clathrin-coated pit necks is required for efficient vesicle uncoating after fission** *Neuron* **72**:587–601

23. Boucrot E., et al. 2015) **Endophilin marks and controls a clathrin-independent endocytic pathway** *Nature* **517**:460–465

24. Renard H. F., et al. 2015) **Endophilin-A2 functions in membrane scission in clathrin-independent endocytosis** *Nature* **517**:493–496

25. Simunovic M., et al. 2017) **Friction Mediates Scission of Tubular Membranes Scaffolded by BAR Proteins** *Cell* **170**:172–184

26. Renard H. F., et al. 2020) **Endophilin-A3 and Galectin-8 control the clathrin-independent endocytosis of CD166** *Nat Commun* **11**:1457

27. Johannes L., Wunder C., Shafaq-Zadah M. 2016) **Glycolipids and Lectins in Endocytic Uptake Processes** *J Mol Biol* **428**:4792–4818

28. Lakshminarayan R., et al. 2014) **Galectin-3 drives glycosphingolipid-dependent biogenesis of clathrin-independent carriers** *Nat Cell Biol* **16**:595–606

29. Lemaigre C., et al. 2023) **N-BAR and F-BAR proteins-endophilin-A3 and PSTPIP1-control clathrin-independent endocytosis of L1CAM** *Traffic* **24**:190–212

30. Arai F., Ohneda O., Miyamoto T., Zhang X. Q., Suda T. 2002) **Mesenchymal stem cells in perichondrium express activated leukocyte cell adhesion molecule and participate in bone marrow formation** *J Exp Med* **195**:1549–1563

31. Ferragut F., Vachetta V. S., Troncoso M. F., Rabinovich G. A., Elola M. T. 2021) **ALCAM/CD166: A pleiotropic mediator of cell adhesion, stemness and cancer progression** *Cytokine Growth Factor Rev* **61**:27–37

32. Weichert W., Knosel T., Bellach J., Dietel M., Kristiansen G. 2004) **ALCAM/CD166 is overexpressed in colorectal carcinoma and correlates with shortened patient survival** *J*

Clin Pathol **57**:1160–1164

33. van Kempen L. C., et al. 2001) **Molecular basis for the homophilic activated leukocyte cell adhesion molecule (ALCAM)-ALCAM interaction** *J Biol Chem* **276**:25783–25790

34. Bowen M. A., et al. 1995) **Cloning, mapping, and characterization of activated leukocyte-cell adhesion molecule (ALCAM), a CD6 ligand** *J Exp Med* **181**:2213–2220

35. Kamoun M., Kadin M. E., Martin P. J., Nettleton J., Hansen J. A. 1981) **A novel human T cell antigen preferentially expressed on mature T cells and shared by both well and poorly differentiated B cell leukemias and lymphomas** *J Immunol* **127**:987–991

36. Aruffo A., et al. 1997) **CD6-ligand interactions: a paradigm for SRCR domain function?** *Immunol Today* **18**:498–504

37. Zimmerman A. W., et al. 2006) **Long-term engagement of CD6 and ALCAM is essential for T-cell proliferation induced by dendritic cells** *Blood* **107**:3212–3220

38. Hassan N. J., Barclay A. N., Brown M. H. 2004) **Frontline: Optimal T cell activation requires the engagement of CD6 and CD166** *Eur J Immunol* **34**:930–940

39. Gimferrer I., et al. 2004) **Relevance of CD6-mediated interactions in T cell activation and proliferation** *J Immunol* **173**:2262–2270

40. Van Seventer G. A., Shimizu Y., Horgan K. J., Shaw S. 1990) **The LFA-1 ligand ICAM-1 provides an important costimulatory signal for T cell receptor-mediated activation of resting T cells** *J Immunol* **144**:4579–4586

41. Zuckerman L. A., Pullen L., Miller J. 1998) **Functional consequences of costimulation by ICAM-1 on IL-2 gene expression and T cell activation** *J Immunol* **160**:3259–3268

42. Deeths M. J., Mescher M. F. 1999) **ICAM-1 and B7-1 provide similar but distinct costimulation for CD8+ T cells, while CD4+ T cells are poorly costimulated by ICAM-1** *European Journal of Immunology* **29**:45–53

43. Johannes L., Shafaq-Zadah M. 2013) **SNAP-tagging the retrograde route** *Methods Cell Biol* **118**:139–155

44. Shafaq-Zadah M., Dransart E., Johannes L. 2021) **Quantitative Methods to Study Endocytosis and Retrograde Transport of Cargo Proteins** *Methods Mol Biol* **2233**:53–70

45. Lehmann F., et al. 1995) **Differences in the antigens recognized by cytolytic T cells on two successive metastases of a melanoma patient are consistent with immune selection** *Eur J Immunol* **25**:340–347

46. Hierro A., et al. 2007) **Functional architecture of the retromer cargo-recognition complex** *Nature* **449**:1063–1067

47. Bugarcic A., et al. 2011) **Vps26A and Vps26B subunits define distinct retromer complexes** *Traffic* **12**:1759–1773

48. Kerr M. C., et al. 2005) **A novel mammalian retromer component, Vps26B** *Traffic* **6**:991–1001

49. Fourriere L., et al. 2019) **RAB6 and microtubules restrict protein secretion to focal adhesions** *J Cell Biol* **218**:2215–2231

50. Mallard F., et al. 2002) **Early/recycling endosomes-to-TGN transport involves two SNARE complexes and a Rab6 isoform** *J Cell Biol* **156**:653–664

51. Tyckaert F., Zanin N., Morsomme P., Renard H. F. 2022) **Rac1, the actin cytoskeleton and microtubules are key players in clathrin-independent endophilin-A3-mediated endocytosis** *J Cell Sci* **135**

52. Baurain J. F., et al. 2000) **High frequency of autologous anti-melanoma CTL directed against an antigen generated by a point mutation in a new helicase gene** *J Immunol* **164**:6057–6066

53. Kjaerulff O., Brodin L., Jung A. 2011) **The structure and function of endophilin proteins** *Cell Biochem Biophys* **60**:137–154

54. Traub L. M., Bonifacino J. S. 2013) **Cargo recognition in clathrin-mediated endocytosis** *Cold Spring Harb Perspect Biol* **5**

55. Moreno-Layseca P., et al. 2021) **Cargo-specific recruitment in clathrin- and dynamin-independent endocytosis** *Nat Cell Biol* **23**:1073–1084

56. Tang Y., et al. 1999) **Identification of the endophilins (SH3p4/p8/p13) as novel binding partners for the beta1-adrenergic receptor** *Proc Natl Acad Sci U S A* **96**:12559–12564

57. Soubeyran P., Kowanetz K., Szymkiewicz I., Langdon W. Y., Dikic I. 2002) **Cbl-CIN85-endophilin complex mediates ligand-induced downregulation of EGF receptors** *Nature* **416**:183–187

58. Petrelli A., et al. 2002) **The endophilin-CIN85-Cbl complex mediates ligand-dependent downregulation of c-Met** *Nature* **416**:187–190

59. Genet G., et al. 2019) **Endophilin-A2 dependent VEGFR2 endocytosis promotes sprouting angiogenesis** *Nat Commun* **10**:2350

60. Steinberg F., et al. 2013) **A global analysis of SNX27-retromer assembly and cargo specificity reveals a function in glucose and metal ion transport** *Nat Cell Biol* **15**:461–471

61. Mallam A. L., Marcotte E. M. 2017) **Systems-wide Studies Uncover Commander, a Multiprotein Complex Essential to Human Development** *Cell Syst* **4**:483–494

62. Wan C., et al. 2015) **Panorama of ancient metazoan macromolecular complexes** *Nature* **525**:339–344

63. Singla A., et al. 2019) **Endosomal PI(3)P regulation by the COMMD/CCDC22/CCDC93 (CCC) complex controls membrane protein recycling** *Nat Commun* **10**:4271

64. Chen K. E., Healy M. D., Collins B. M. 2019) **Towards a molecular understanding of endosomal trafficking by Retromer and Retriever** *Traffic* **20**:465–478

65. Fuse A., et al. 2015) **VPS29-VPS35 intermediate of retromer is stable and may be involved in the retromer complex assembly process** *FEBS Lett* **589**:1430–1436

66. Shi G., et al. 2012) **SNAP-tag based proteomics approach for the study of the retrograde route** *Traffic* **13**:914–925

67. Degiovanni G., Lahaye T., Hérin M., Hainaut P., Boon T. 1988) **Antigenic heterogeneity of a human melanoma tumor detected by autologous CTL clones** *European Journal of Immunology* **18**:671–676

68. Stringer C., Pachitariu M. 2024) **Cellpose3: one-click image restoration for improved cellular segmentation** *bioRxiv* https://doi.org/10.1101/2024.02.10.579780

Author information

Shiqiang Xu
UNamur, Namur Research Institute in Life Sciences, Research Unit in Cell Biology, Namur, Belgium, UCLouvain, Louvain Institute of Biomolecular Science and Technology, Group of Molecular Physiology, Louvain-la-Neuve, Belgium
ORCID iD: 0000-0002-0696-499X

Alix Buridant
UNamur, Namur Research Institute in Life Sciences, Research Unit in Cell Biology, Namur, Belgium

Thibault Hirsch
UCLouvain, de Duve Institute, Bruxelles, Belgium
ORCID iD: 0000-0002-4448-1948

Massiullah Shafaq-Zadah
Institut Curie, PSL Research University, Cellular and Chemical Biology unit, U1143 INSERM, UMR3666 CNRS, Paris, France
ORCID iD: 0000-0002-7582-8131

Estelle Dransart
Institut Curie, PSL Research University, Cellular and Chemical Biology unit, U1143 INSERM, UMR3666 CNRS, Paris, France
ORCID iD: 0000-0003-2547-6825

Benjamin Ledoux
UNamur, Morph-Im Platform, Namur, Belgium
ORCID iD: 0009-0004-0336-6478

Ludger Johannes
Institut Curie, PSL Research University, Cellular and Chemical Biology unit, U1143 INSERM, UMR3666 CNRS, Paris, France
ORCID iD: 0000-0002-2168-0004

Pierre van der Bruggen
UCLouvain, de Duve Institute, Bruxelles, Belgium, WELBIO, Wavre, Belgium
ORCID iD: 0000-0002-3910-4101

Pierre Morsomme
UCLouvain, Louvain Institute of Biomolecular Science and Technology, Group of Molecular Physiology, Louvain-la-Neuve, Belgium

ORCID iD: 0000-0001-7780-7230

Henri-François Renard
UNamur, Namur Research Institute in Life Sciences, Research Unit in Cell Biology, Namur, Belgium, UNamur, Morph-Im Platform, Namur, Belgium
ORCID iD: 0000-0002-2406-2519

For correspondence: henri-francois.renard@unamur.be

Editors

Reviewer #1 (Public review):

Summary:

This study by Xu et al. focuses on the impact of clathrin-independent endocytosis in cancer cells on T cell activation. In particular, by using a combination of biochemical approaches and imaging, the authors identify ICAM1, the ligand for T cell-expressed integrin LFA-1, as a novel cargo for EndoA3-mediated endocytosis. Subsequently, the authors aim to identify functional implications for T cell activation, using a combination of cytokine assays and imaging experiments.

They find that the absence of EndoA3 leads to a reduction in T cell-produced cytokine levels. Additionally, they observe slightly reduced levels of ICAM1 at the immunological synapse and an enlarged contact area between T cells and cancer cells. Taken together, the authors propose a mechanism where EndoA3-mediated endocytosis of ICAM1, followed by retrograde transport, supplies the immunological synapse with ICAM1. In the absence of EndoA3, T cells attempt to compensate for suboptimal ICAM1 levels at the synapse by enlarging their contact area, which proves insufficient and leads to lower levels of T cell activation.

Strengths:

The authors utilize a rigorous and innovative experimental approach that convincingly identifies ICAM1 as a novel cargo for Endo3A-mediated endocytosis.

Weaknesses:

The characterization of the effects of Endo3A absence on T cell activation appears incomplete. Key aspects, such as surface marker upregulation, T cell proliferation, integrin signalling and most importantly, the killing of cancer cells, are not comprehensively investigated.

As Endo- and exocytosis are intricately linked with the biophysical properties of the cellular membrane (e.g. membrane tension), which can significantly impact T-cell activation and cytotoxicity, the authors should address this possibility and ideally address it experimentally to some degree.

Crucially, key literature relevant to this research, addressing the role of ICAM1 endocytosis in antigen-presenting cells, has not been taken into consideration.

https://doi.org/10.7554/eLife.105821.1.sa2

Reviewer #2 (Public review):

Summary:

The manuscript by Xu et al. studies the relevance of endophilin A3-dependent endocytosis and retrograde transport of immune synapse components and in the activation of cytotoxic CD8 T cells. First, the authors show that ICAM1 and ALCAM, known components of immune synapses, are endocytosed via endoA3-dependent endocytosis and retrogradely transported to the Golgi. The authors then show that blocking internalization or retrograde trafficking reduces the activation of CD8 T cells. Moreover, this diminished CD8 T cell activation resulted in the formation of an enlarged immune synapse with reduced ICAM1 recruitment.

Strengths:

The authors show a novel EndoA3-dependent endocytic cargo and provide strong evidence linking EndoA3 endocytosis to the retrograde transport of ALCAM and ICAM1.

Weaknesses:

The role of EndoA3 in the process of T cell activation is shown in a cell that requires exogenous expression of this gene. Moreover, the authors claim that their findings are important for polarized redistribution of cargoes, but failed to show convincingly that the cargoes they are studying are polarized in their experimental system. The statistics of the manuscript also require some refinement.

https://doi.org/10.7554/eLife.105821.1.sa1

Reviewer #3 (Public review):

Summary:

Shiqiang Xu and colleagues have examined the importance of ICAM-1 and ALCAM internalization and retrograde transport in cancer cells on the formation of a polarized immunological synapse with cytotoxic CD8+ T cells. They find that internalization is mediated by Endophilin A3 (EndoA3) while retrograde transport to the Golgi apparatus is mediated by the retromer complex. The paper is building on previous findings from corresponding author Henri-François Renard showing that ALCAM is an EndoA3-dependent cargo in clathrin-independent endocytosis.

Strengths:

The work is interesting as it describes a novel mechanism by which cancer cells might influence CD8+ T cell activation and immunological synapse formation, and the authors have used a variety of cell biology and immunology methods to study this. However, there are some aspects of the paper that should be addressed more thoroughly to substantiate the conclusions made by the authors.

Weaknesses:

In Figure 2A-B, the authors show micrographs from live TIRF movies of HeLa and LB33-MEL cells stably expressing EndoA3-GFP and transiently expressing ICAM-1-mScarlet. The ICAM-1 signal appears diffuse across the plasma membrane while the EndoA3 signal is partially punctate and partially lining the edge of membrane patches. Previous studies of EndoA3-mediated endocytosis have indicated that this can be observed as transient cargo-enriched puncta on the cell surface. In the present study, there is only one example of such an ICAM-1 and EndoA3 positive punctate event. Other examples of overlapping signals between ICAM-1 and EndoA3 are shown, but these either show retracting ICAM-1 positive membrane protrusions or large membrane patches encircled by EndoA3. While these might represent different modes of EndoA3-mediated ICAM-1 internalization, any conclusion on this would require further investigation.

Moreover, in Figure 2C-E, uptake of the previously established EndoA3 endocytic cargo ALCAM is analyzed by quantifying total internal fluorescence in LB33-MEL cells of antibody labelled ALCAM following both overexpression and siRNA-mediated knockdown of EndoA3, showing increased and decreased uptake respectively. Why has not the same quantification been done for the proposed novel EndoA3 endocytic cargo ICAM-1? Furthermore, if endocytosis of ICAM-1 and ALCAM is diminished following EndoA3 knockdown, the expression level on the cell surface would presumably increase accordingly. This has been shown for ALCAM previously and should also be quantified for ICAM-1.

In Figure 4A the authors show micrographs from a live-cell Airyscan movie (Movie S6) of a CD8+ T cell incubated with HeLa cells stably expressing HLA-A*68012 and transiently expressing ICAM1-EGFP. From the movie, it seems that some ICAM-1 positive vesicles in one of the HeLa cells are moving towards the T cell. However, it does not appear like the T cell has formed a stable immunological synapse but rather perhaps a motile kinapse. Furthermore, to conclude that the ICAM-1 positive vesicles are transported toward the T cell in a polarized manner, vesicles from multiple cells should be tracked and their overall directionality should be analyzed. It would also strengthen the paper if the authors could show additional evidence for polarization of the cancer cells in response to T-cell interaction.

Finally, in Figures 4D-G, the authors show that the contact area between CD8+ T cells and LB33-MEL cells is increased in response to siRNA-mediated knockdown of EndoA3 and VPS26A. While this could be caused by reduced polarized delivery of ICAM-1 and ALCAM to the interface between the cells, it could also be caused by other factors such as increased cell surface expression of these proteins due to diminished endocytosis, and/or morphological changes in the cancer cells resulting from disrupted membrane traffic. More experimental evidence is needed to support the working model in Figure 4H.

https://doi.org/10.7554/eLife.105821.1.sa0